JPL Publication 17-2

The JPL Neptune Radiation Model (NMOD)

Henry Garrett
Jet Propulsion Laboratory
California Institute of Technology
Pasadena, California

Robin Evans
Bastion Technologies
Houston, Texas

National Aeronautics and
Space Administration

Jet Propulsion Laboratory
California Institute of Technology
Pasadena, California

July 1, 2017

This research was carried out at the Jet Propulsion Laboratory, California Institute of Technology, under a contract with the National Aeronautics and Space Administration.

Acknowledgments

The inspiration for this study was our colleague N. Divine. The authors would also like to thank M. Boyles and H. Schone for their interest in funding and having the NMOD radiation model made available for general JPL use. I. Jun, L. M. Martinez Sierra, M. de Soria-Santacruz-Pich, and W. Kim as always have provided important and critical feedback on the model and its applications. We would also like to acknowledge the Voyager team's outstanding success at Neptune that made this study possible. In particular, we would like to thank B. Mauk and M. Looper for their valuable inputs on the Voyager data. Finally, Roger Carlson, as in the past, has been our faithful editor, formatter, and proofreader.

Table of Contents

Figures

Tables

Abstract

The objective of this study is the development of a comprehensive radiation model of the Neptunian environment for JPL mission planning. The ultimate goal is to provide a description of the high-energy electron and proton environments and the magnetic field at Neptune that can be used for engineering design. The JPL Neptune Radiation Model (NMOD) models the high-energy electrons and protons between 0.025 MeV and 5 MeV based on the California Institute of Technology's Cosmic Ray Subsystem and the Applied Physics Laboratory's Low Energy Charged Particle Detector on Voyager 2. As in previous JPL radiation models, the form of the Neptunian model is based on magnetic field coordinates and requires a conversion from spacecraft coordinates to Neptunian-centered magnetic "B-L" coordinates. Two types of magnetic field models have been developed for Neptune: 1) simple "offset, tilted dipoles" (OTD), and 2) a complex, multi-pole expansion model ("O_8"). A review of the existing data on Neptune and a search of the NASA Planetary Data System (PDS) were completed to obtain the most current descriptions of the Neptunian high-energy particle environment. These data were fit in terms of the O_8 B-L coordinates to develop the electron and proton flux models. The flux predictions of the new model were used to estimate the total ionizing dose (TID) rate along the Neptunian equator, meridional flux contours for the electrons and protons, and for flux and dose comparisons with the other radiation belts in the Solar System.

1. Introduction

Figure 1, from the Voyager 2 flyby, shows Neptune, its clouds, and the moon Triton. As noted in the last Planetary Decadal Survey (*Vision and Voyages for Planetary Science in the Decade 2013-2022;* National Academy of Sciences, 2011) by the National Research Council, Uranus and Neptune, the next giant planets after Jupiter and Saturn, differ dramatically from them and are "a wholly distinct class of planet." As illustrated in Fig. 2, because of its highly tilted magnetic field, Neptune has a unique magnetospheric configuration and interaction with the Solar Wind. A Neptune Orbiter and Probe Flagship Mission to explore the planet and its interactions have been considered as possible JPL missions. To design a successful spacecraft mission, knowledge of the Neptunian environment, particularly its magnetic field and radiation belts, is required to determine the required radiation shielding.

Voyager 2 flew within 107,000 km of Neptune on August 24–25, 1989. During this flyby, several instruments on board measured the trapped radiation at Neptune. This radiation environment, while relatively mild compared to that at the Earth, Saturn, and Jupiter, represents a basically unknown potential threat to future missions to Neptune. The purpose of this study is to revisit the original analyses of the Voyager team (Mauk et al., 1991, 1994, 1995; Stone et al., 1989; Connerney et al., 1991; Looper, 1993) and, based on published findings, provide a simple computer model for the Neptunian radiation environment that can be used for mission planning. As mentioned, Neptune has been proposed as a potential Outer Planets target, and several recent Neptune mission studies have been completed by JPL and other centers (see Hofstdater et al., 2017)—but without any consideration of the radiation environment. Neptune, because of its tilted magnetic field (almost 47°) to the spin axis) and its inclined spin axis (~29°), (see Fig. 2) represents a challenge compared to previous radiation belt models. To develop a working model

of this complex environment requires a model of the electron and proton particle fluxes versus pitch angle and energy. These are given in terms of magnetic field coordinates (B-L). Spacecraft location in a Neptunian-centric system is then transformed into B-L coordinates. Once the position of the spacecraft in magnetic coordinates is determined, the observed particle fluxes are fit as functions of energy, pitch angle, and B-L. The details of these fitting processes, a review of the data, and a description of the final Neptune radiation model in the form of a FORTRAN code, NMOD, for simulating the Neptunian environment are presented in the following.

Figure 1. Voyager 2 composite image of Neptune and its moon Triton (credit: JPL; also see Smith et al., 1989).

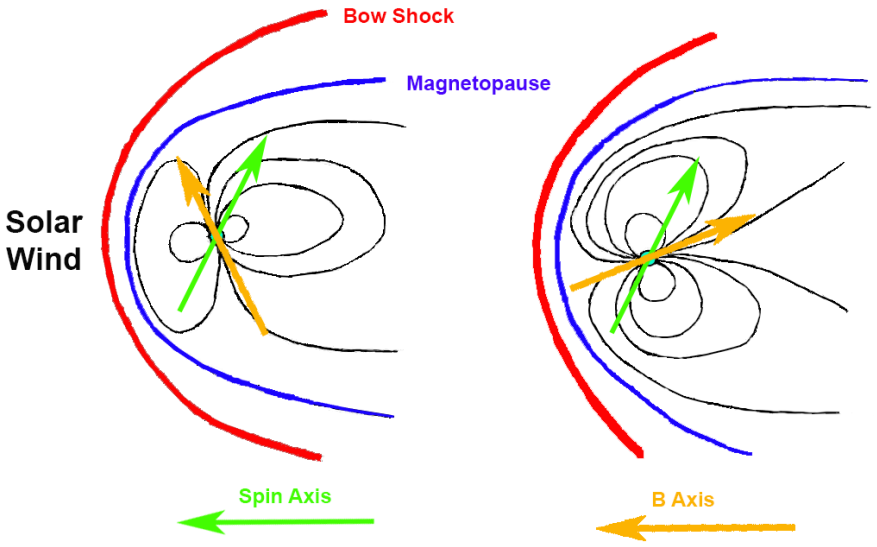

Figure 2. Schematic representations of Neptune's magnetic field and magnetosphere showing the complex relationship between its highly tilted magnetic field and the solar wind (after Bagenal, 1992).

The first step in analyzing the Neptunian data is to establish as accurately as possible the location of Voyager relative to Neptune. In generating the position data for Voyager 2 and modeling the Neptunian magnetic field, a major difficulty is the uncertainty in two very basic quantities—the planetary rotation rate and the location of the "0°" longitude. In the case of Neptune, some of the Voyager observations have taken a very long time to get "in the textbooks." Thus, any analysis of the Voyager Neptune data entails some "forensic" investigation to set the stage for further studies. In the process of performing that study, Evans (Evans, 2017a) found that the definition of the Neptunian coordinate system (as was the case for Uranus) at the time of the fly-by was different from that currently used by the JPL Spacecraft Planets Instrument C-Matrix Events (SPICE) system (the SPICE ancillary information system, part of NASA's Navigation and Ancillary Information Facility (NAIF), is used to compute the trajectories and other geometric information used in analyzing science observations). To adequately address this issue, a detailed discussion is presented of the steps performed in regenerating the PDS coordinates used by the original Voyager investigators from the SPICE coordinates.

2. Rotation Rate and 0° Longitude

The Voyager 2 flyby of Neptune predated the creation of SPICE. A retrofit of the Voyager tracking to agree with SPICE was created. The retrofitted coordinates were then verified by comparison to published data (see below). During its encounter, the Voyager team defined a planetary coordinate system such that, at closest approach on 1989 August 25 03:55:39 UT, the spacecraft sub-West Longitude was defined to be at 167.7°. Voyager also determined the rotation rate of Neptune to be 536.3128° per 24-hour day, giving a 16.11 hour Neptune day (Warwick et al., 1989). A previous measurement was 468.75° per day (14.16-hour day) which was the official International Astronomical Union (IAU) value until 2005. As NAIF used the IAU as a source for planetary constants, the early SPICE system did not have the correct rotation rate when the Voyager data were retrofit as the corrected rotation rate was only adopted by the

IAU and SPICE the next year. This means SPICE should (in principal) reproduce the Voyager coordinate system, but it does not. As will be demonstrated in the next section, to correct the SPICE trajectory coordinates for use with the Voyager 2 data, 12.0° has to be added to the SPICE value of West longitude. (While other methods of correcting the SPICE coordinates for Voyager 2 were considered, this was found to be the simplest way to correct the data). An alternative is to alter the planetary constants file to produce the correct West longitudes. This was done with Uranus but it is problematic in that the altered planetary constants file has to be supplied with the magnetic field model. Uranus was also more complicated in that the IAU also flipped Uranus upside down to get the north spin pole to lie north of the ecliptic. This was not necessary for Neptune whose axial tilt is more normal to the Ecliptic Plane.

3. Magnetic Field Models

To get the Neptune magnetic field model predictions (see descriptions of the magnetic field models below) to agree with the PDS magnetic field measurements, the SPICE longitude coordinates had to be modified. The "correction" angle was found by varying the reported PDS SPICE spacecraft longitude from 0° to 17° W when using the Connerney O_8 model (Connerney et al., 1987; Connerney, 1993). The data show a peak at 9923 nT on 1989 August 25 (Day 237) at 03:49:00, a local minimum of 9185 nT at 03:53:30, and a second peak of 9743 nT at 03:58:30. Assuming 150.7° W (e.g., using the original SPICE coordinates) is the closest approach longitude in the model gives a single large peak on Day 237 at 03:50:16 (there is no local minimum or second peak). A longitude for closest approach of 162.7° W gives two peaks and a local minimum of approximately the correct ratio of size and time. The times are 237 3:50:17, 237 3:57:10, and 237 4:03:33, respectively, and they are off by 1 minute, 4 minutes, and 5 minutes, respectively. The time for the first peak does not change as the West longitude is varied by up to 12° but then increases rapidly after that. The amplitude decreases linearly with angle over the complete range while the times for the local minimum change linearly with West longitude. The amplitude increases as a quadratic function with angle for the complete range. The times for the second peak increase as a log function as the West longitude is varied. Finally, the amplitude increases linearly with angle for the complete range.

To demonstrate these findings, Fig. 3 compares the PDS magnetic field data (B(PDS)) to the magnetic field model predictions using the original SPICE spacecraft coordinates (B0) and the SPICE coordinates shifted by 12° W in longitude in the O_8 model (B12), the OTD2 magnetic field model (OTD2_12), and the ED2 magnetic field model (ED2_12)—the latter two both displaced by 12° W (these magnetic field models are described below). The line, CA, is the time of closest approach. Only the O_8 model produces both peaks, and the +12° W shift gives the best fit. Note that the single dipole model peaks are near the second peak.

One of the earliest magnetic models used by the Voyager team was an Offset Tilted Dipole (OTD, Ness et al., 1989). This model fit assumed that the closest approach was at 1989 Aug 25 03:55:39 160° W and that the closest approach was at 1.18 R_N (R_N = 24,765 km)—the North pole for this model was at 79.5° W longitude/46.8° colatitude with a dipole magnitude of 0.133G-R_N^3 and centered at 0.55 R_N. Next, a spherical harmonic model was produced [Connerney et al., 1991]. This is the "I8E1 44 ev" magnetic field model. Unfortunately, several of the harmonic coefficients were not well constrained in this early model. For this model, the closet approach was assumed to occur on 1989 Aug 25 03:56:00 at 167.7° W and at 1.18 R_N. An eccentric dipole model based on this model, called ED2, was also developed. Next, the fitting

terms for the spherical model were refined to produce the final O_8 field model. The O_8 model has an equivalent dipole of 0.14 G-R_N^3 tilted by 46.9° towards 72° W longitude and displaced along the rotation axis by 0.33 R_N (ED2 or OTD O_8).

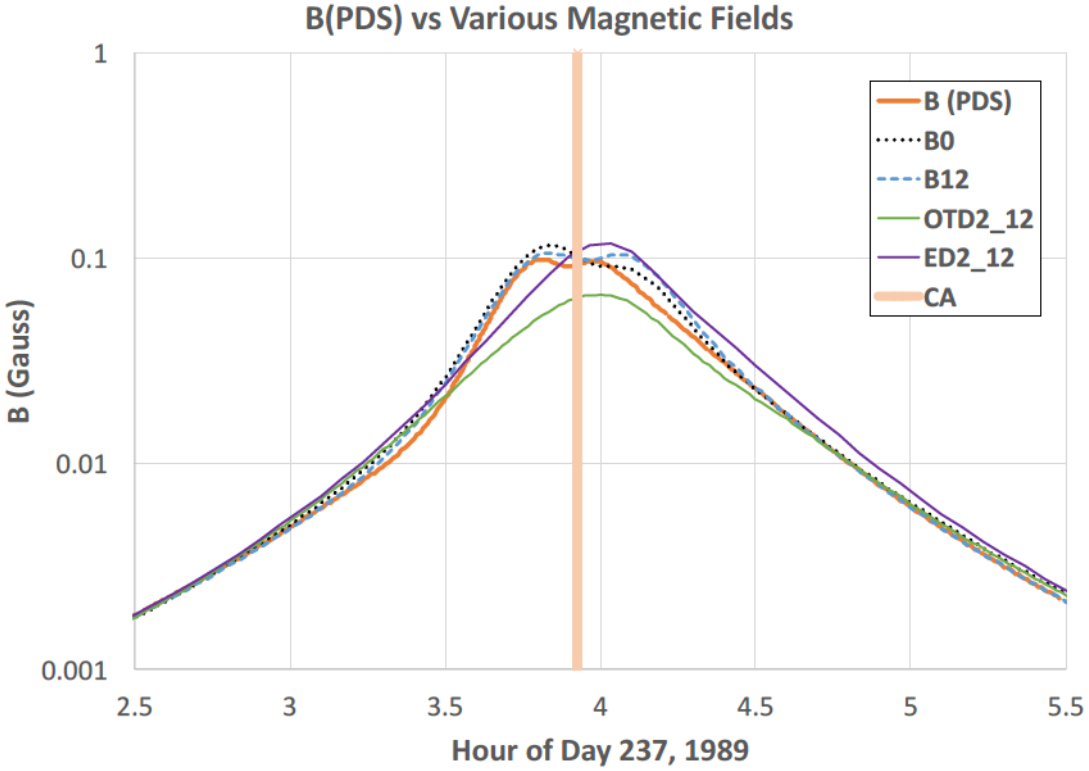

Figure 3. Comparison of PDS magnetic field data and magnetic field model predictions from SPICE (B0), SPICE + 12° W longitude (B12), OTD2 + 12° W longitude (OTD2_12), and ED2 + 12° W longitude (ED2_12). CA is the time of closest approach.

Several other Neptune dipole models have also been presented in the literature including an eccentric dipole model, called here "EDM" (Connerney, 1993). Two related reference dipole models are the "OTD2" and "DP" models (Ness et al., 1996). The OTD2 model was used in early Neptune papers (referred to as a private communication in Acuna et al. (1993)) but was not published until Ness et al. (1996). The DP model is also a dipole but is not offset from the center of the planet—it was derived from the I8E1-44 ev model (Ness et al. [1996], Table III). Table 1 lists the various parameters for all the Neptune dipole models considered in this study along with the OTD models for Jupiter and Uranus for comparison. Parameters are given as a magnitude and as vector components in planetocentric coordinates. Parameters in green are used to calculate the magnetic equator field value (B_{eq}) and parameters in red are used to calculate the dipole field value (B_{sc}). Table 2 lists the parameters used for the O_8 model. This full octupole model, O_8, is by far the most accurate of the B-field models and is the primary magnetic field model used in this study.

Table 1. Parameters of Five Dipole Magnetic Field Models of Neptune's Magnetic Field. Jupiter and Uranus are listed for comparison.

	Jupiter	Uranus	N(OTD)	N(EDM)	N(OTD2)	N(DP)	N(ED2) or OTD(O_8)
Offset							
Magnitude	0.101	0.310	0.5500	0.4850	0.5501	0.0000	0.4826
Rx	-0.092	-0.020	0.1700	**0.0470**	0.1900	0.0000	**0.0500**
Ry	-0.042	0.020	0.4600	0.4830	0.4800	0.0000	0.4800
Rz	0.009	-0.310	-0.2400	**0.0020**	-0.1900	0.0000	**0.0000**
Mag Vector							
Colat	10.770	60.000	46.8000	46.9000	45.2000	46.9000	46.9000
Wlong	200.800	48.000	79.5000	72.0000	76.5000	72.0000	72.0000
Magnitude	4.225	0.230	0.1330	0.1420	0.1300	0.1420	0.1420
AMx	-0.738	0.133	0.0177	0.0320	0.0215	0.0320	0.0320
AMy	0.280	-0.148	-0.0953	-0.0986	-0.0897	-0.0986	-0.0986
AMz	4.151	0.115	0.0910	0.0970	0.0916	0.0970	0.0970

Table 2. Spherical Harmonic Parameters for the O_8 Model.

Parameter	Value (G)
g10	0.0973
g11	0.0322
g20	0.0745
g21	0.0066
g22	0.0450
g20	-0.0659
g31	0.0410
g32	-0.0358
g33	0.0048
h11	-0.0989
h21	0.1123
h22	-0.0007
h31	-0.0367
h32	0.0179
h33	-0.0077

Figure 4 shows the magnetic field magnitude for the O_8 and five dipole models for the Voyager 2 flyby. Note that the O_8 model has two local maxima near closest approach where the dipoles have only a single large peak. This double peak was a surprise to the Voyager particle scientist who had found a similar double peak in the particle data before the O_8 model became available. The two eccentric dipole models fit the O_8 model best. Figure 5 shows the McIlwain L parameter determined by the six models for the Voyager 2 trajectory. No dipole model fits the O_8 model very well, but all agree approximately over small ranges. Again, note the double peak in the O_8 model.

Figure 6A plots the relationship of B to L-shell for the O_8 model (B-L(O8) is for the original SPICE longitudes and the O_8 model while B-L(O8)+12 uses the SPICE West longitude plus 12°) overlaid on data from a published plot—Fig. 5 from Mauk et al. (1995)—of B vs L for the Neptune flyby. Clearly, the JPL FORTRAN version of the O_8 field model closely reproduces this figure when the 12° longitude shift is included.

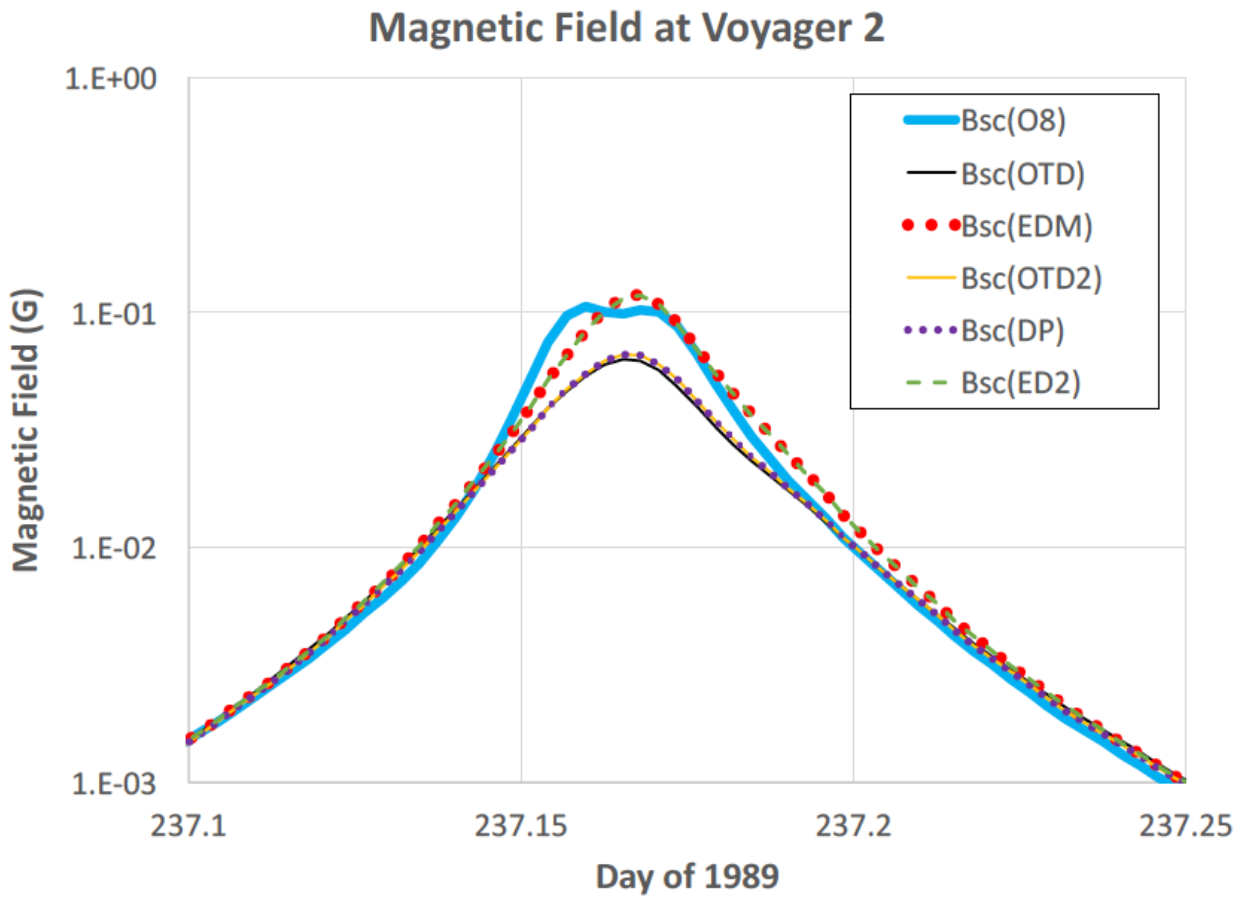

Figure 4. Magnetic field versus time for the six models.

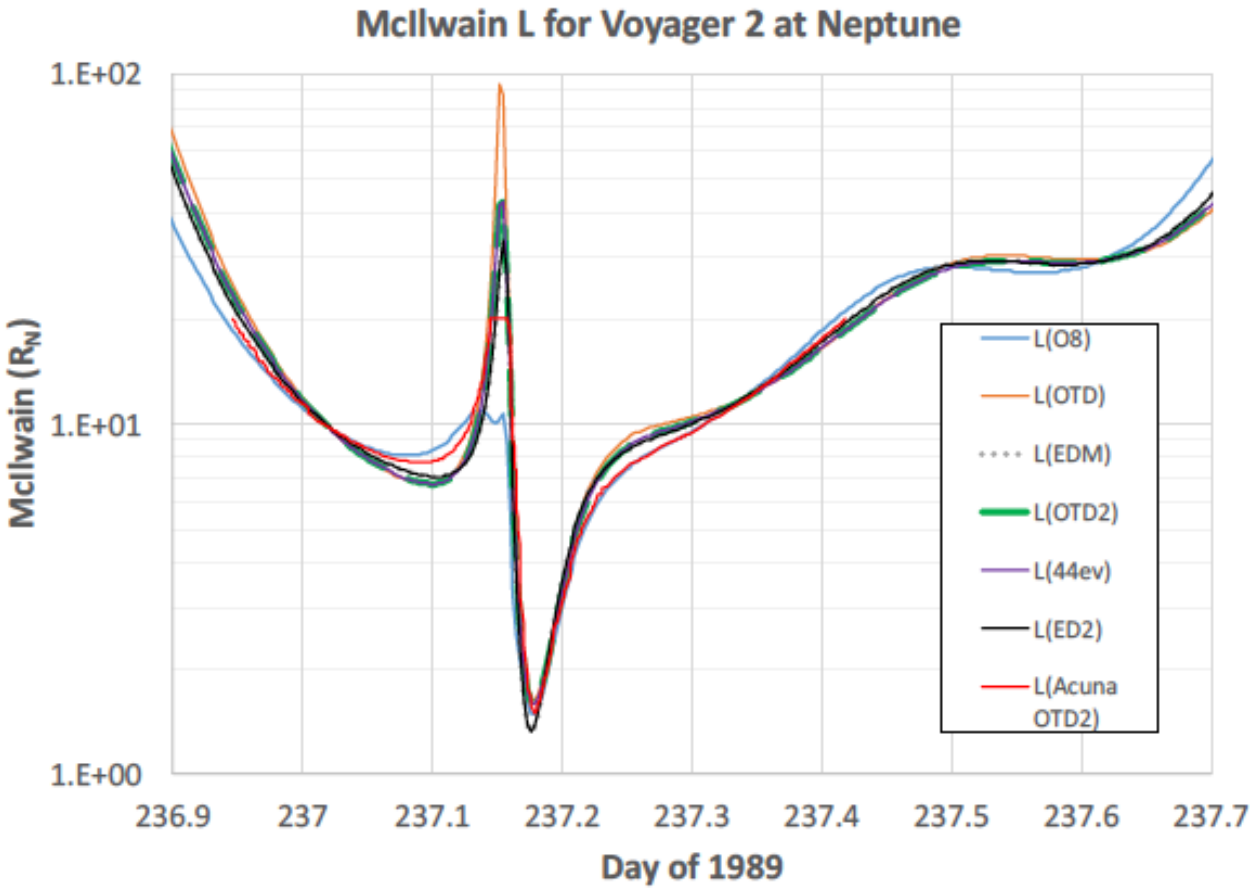

Figure 5. McIlwain L parameter from six magnetic field models.

Fig. 6B compares the OTD models in Table 1 with the O_8+12 model in terms of B vs L. None of these OTD models was found to agree with the O_8 model. To reproduce the upper bound on the B vs L plot, the magnetic dipole has to be displaced towards the position of Voyager's closest approach by an additional 0.25 R_N from the models' displacement positions. Modifying the magnetic dipole strength (components) by varying amounts reduced the large rightward spike on the top right of the curves in Fig. 6B but ultimately was not successful in reproducing the O_8 curve in Fig. 6A. There are apparently more OTD versions of the Neptune magnetic field then those listed in Table 1 as Mauk et al.'s (1995) "OTD2" in their Fig. 5 plot agrees much better with the O_8 model than any of the OTD models in Fig. 6B—we were unable, however, to reproduce that model plot.

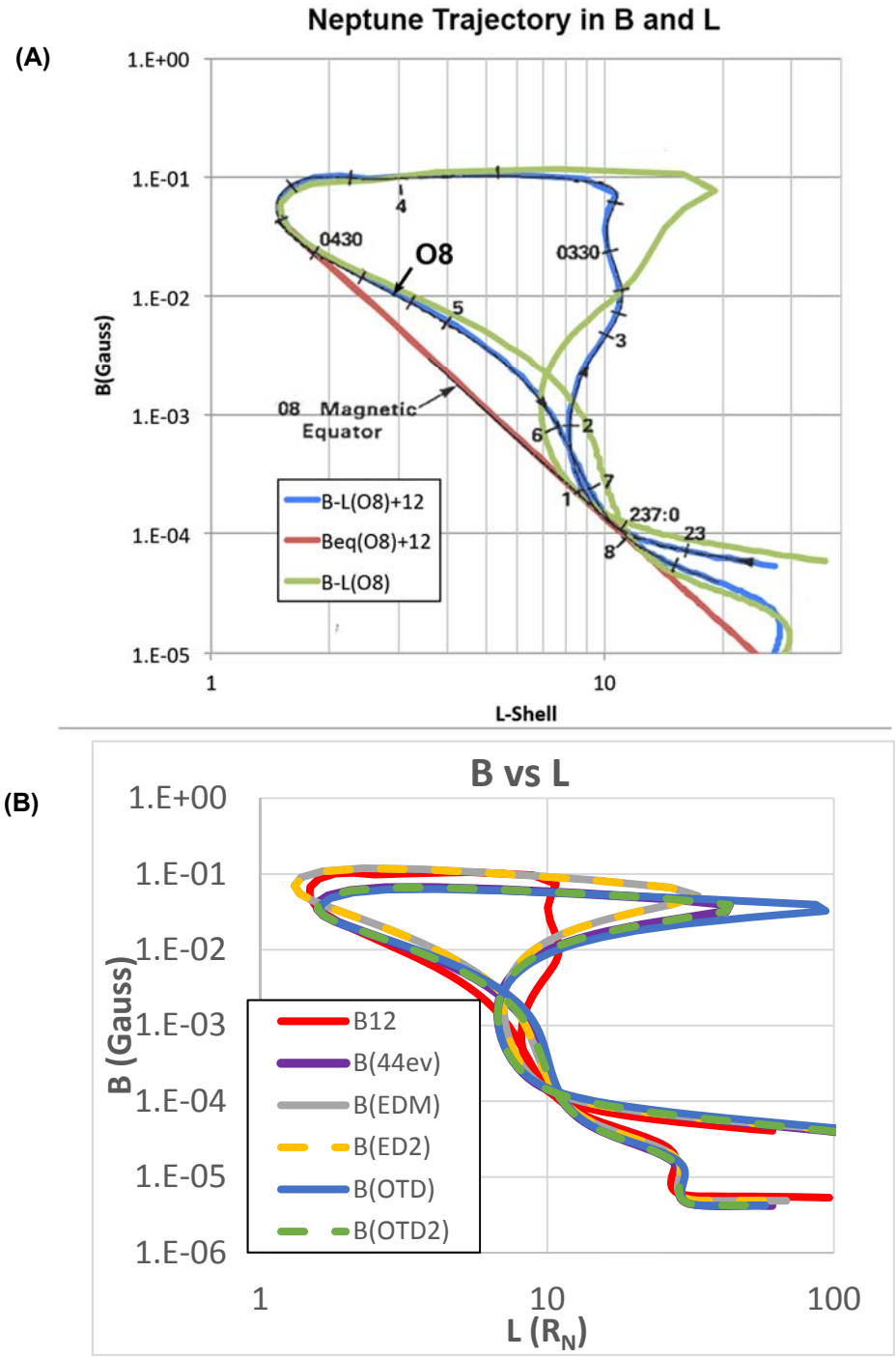

Figure 6. Comparisons of various magnetic field models with a similar curve from Mauk et al. (1995) (their Fig. 4-black line with tic marks). (A) Plotted is the Voyager 2 trajectory at Neptune in B,L coordinates for the O_8 at the SPICE West longitude (B-L(O8)) and for the O_8 model using the SPICE West longitude plus 12° (B-L(O8)+12). Beq(O8)+12 is the field strength along the magnetic equator for West longitude +12°. (B) B versus L for 5 OTD models and the O_8 (B12) model.

Figure 7 compares Connerney's surface contours (Connerney, 1993) with the JPL O_8 surface model contours. Connerney's are the black contour lines and JPL's are the color contours. This is for a pole flattened Neptune. The magnetic dip equator is also in Connerney's plot. Circle-cross and circle-dot are the dipole pole locations (Dot=North, Cross=South).

Figure 8 shows the L surface contours. Connerney's magnetic field B contours are the black contour lines while JPL color contours correspond to the L-shell contours. This is again for a pole flattened Neptune. The magnetic dip equator is also shown in Connerney's plot—note that this contour appears to pass through the lowest L values as would be expected while the highest L values are near the apparent magnetic poles. The two "cross-hatched" auroral oval regions in the Connerney plot overlay the maximum L-shell contours. As before, circle-cross and circle-dot are the dipole pole locations, Dot = North, Cross = South.

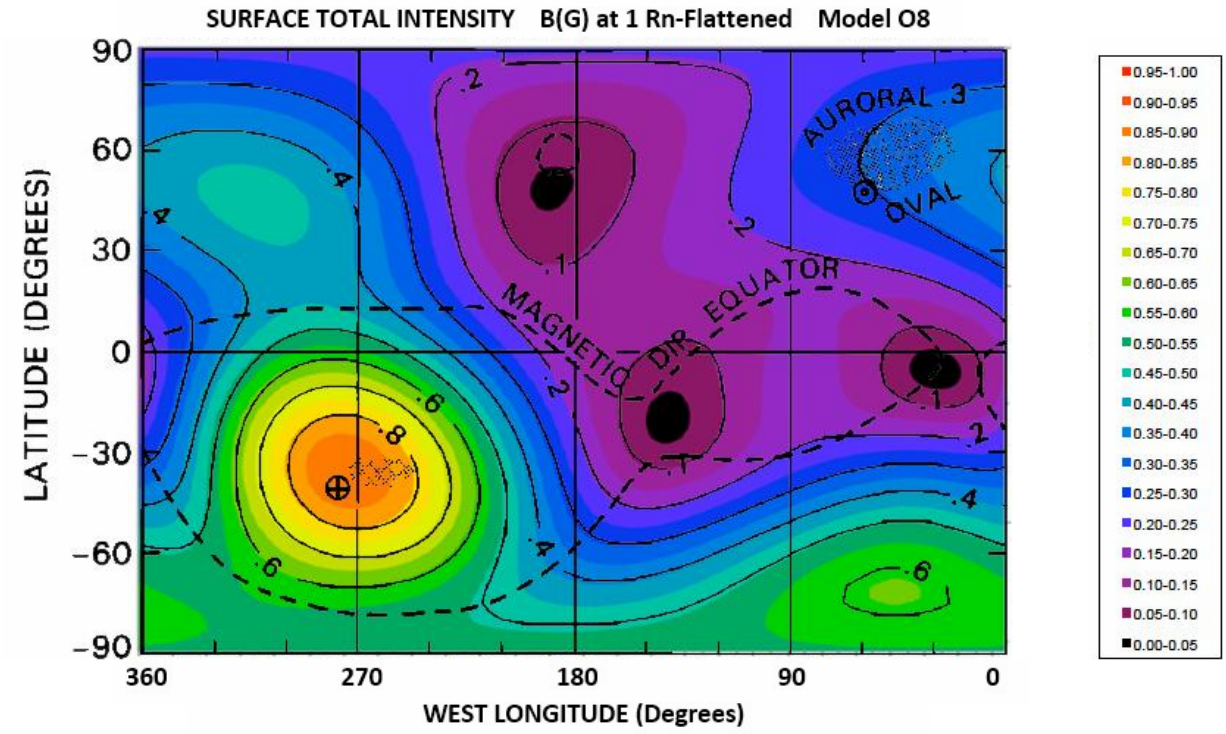

Figure 7. Comparison of Connerney's published contours (Connerney, 1993) and the report's contours for O_8. Connerney is in black, the report is in color. Color contour levels are in gauss.

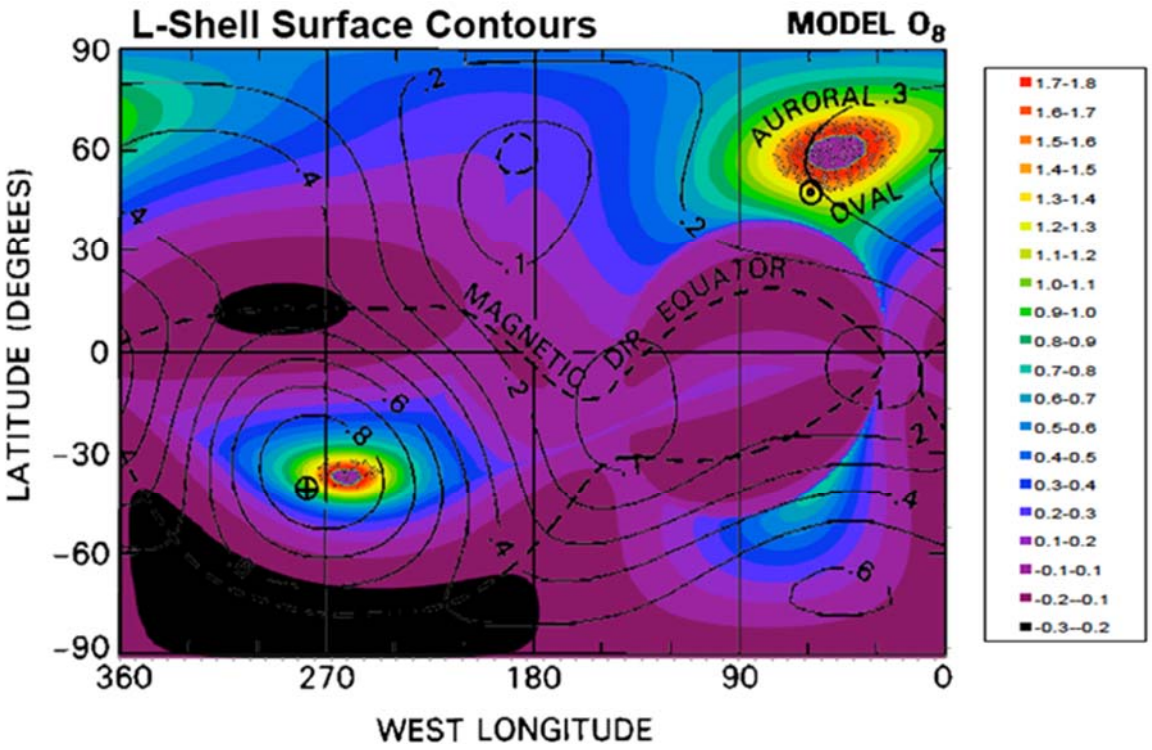

Figure 8. Comparison of L-shell contours for the Connerney O_8 model (Connerney, 1993). Original Connerney is in black, and this study's results are in color. Color contour levels are Log_{10}(L).

4. Voyager 2 High Energy Electron Radiation Model

The first charged particle component of the NMOD is based on measurements from the Voyager 2 cosmic ray system (CRS) [Stone et al., 1977]. Specifically, the energetic electron model at Neptune is based on flyby data from two sensors on the electron telescope (TET) which was part of the CRS. The instrument provided estimates of the fluxes between ~1.0 MeV to ~2.5 MeV and for L-shell values between ~1.5 and 25 (based on the O_8 magnetic field model). Stone et al. (1989) has provided the electron differential intensity during the flyby as a function of energy assuming that the flux varies approximately with a power law in energy ($E^{-\gamma}$). That is:

$$f(E) = A_0 E^{-\gamma} \qquad (1)$$

where:

$f(E)$	= electron differential intensity at equator, $(cm^2\text{-sr-s-MeV})^{-1}$, with energy; assumed to vary as $\sim A_0 E^{-\gamma}$ at the magnetic equator as in Selesnick and Stone's Uranian model (Selesnick and Stone, 1991)
A_0, γ	= constants
E	= energy (MeV)
"0"	= subscript "0" refers to equatorial values

The local values measured at the spacecraft are related to the equatorial values by the following:

$$\sin^2 \alpha = \frac{B}{B_0} \sin^2 \alpha_0 \tag{2}$$

$$A = \left[\frac{B_0}{B} \right]^n A_0 \tag{3}$$

where:

α	= pitch angle of particle relative to magnetic field direction at spacecraft location
n	= constant; assumed to be 0 in Stone et al. [1989] which gives an isotropic distribution for the high-energy electron population
B	= magnitude of magnetic field at location
B_0	= magnitude of magnetic field at magnetic equator
A	= equivalent of A_0 in Eq. 1 at the spacecraft location

Stone et al. (1989) estimated the above constants at the magnetic equator (A_0) as functions of the magnetic L-shell based on fits to the Voyager data. Their values are listed in Table 3. A FORTRAN program was written that takes the values in Table 3 and (given Equations 1, 2, and 3) computes the differential electron intensity for a given B and L value. To compute the electron intensities for a trajectory or at a given spatial location around Neptune, B and L are calculated—using Eq. 1 these then give the electron isotropic intensities at the B and L location(s) versus energy. The electron spectra have been extrapolated to provide estimates up to 5 MeV.

Table 3. Coefficients derived from the Stone et al. (1989) model of the Neptunian electron environment used in Eq. 1 to compute the electron differential intensity versus energy (1–2.5 MeV). Pitch angle distribution assumed isotropic.

Day	A0	Gamma
236.9896	80.0000	5.8000
236.9978	350.5196	6.3010
237.0091	1014.6223	6.1207
237.0181	2510.5019	6.2168
237.0386	6512.0845	5.9125
237.0481	8386.7722	5.5856
237.0579	9008.8899	5.3320
237.0687	9219.5263	5.1968
237.0780	8261.8241	5.1970
237.0882	6559.6588	5.4058
237.0984	3250.1515	6.1954
237.1083	1497.748	5.7106
237.1380	825.8423	5.6941
237.1488	739.9037	5.6941
237.1882	239.4437	4.7137
237.1985	1414.5920	6.2646
237.2081	4298.3140	5.9489
237.2178	1177.7333	6.3325
237.2276	9881.0418	5.3007
237.2376	16804.6368	4.6467
237.2478	11967.2591	4.4101
237.2584	11810.8047	5.0982
237.2775	6363.3044	5.2169
237.2879	4422.7561	5.4708
237.2979	2824.8861	5.8206
237.3083	1657.8114	6.0012
237.3178	745.7076	5.8604
237.3275	339.5102	6.3567
237.3374	110.1737	6.1539

5. Voyager 2 High-Energy Proton Radiation Model

The Voyager 2 CRS (Stone et al., 1977) also observed the high-energy proton environment. The CRS Low Energy Telescopes (LET) measured the proton environment between 1.9 to 5.0 MeV at Neptune for L-shell values between ~1.5 and 25 (based on the O_8 magnetic field model). Looper in his thesis (Looper, 1993) has provided a detailed analysis of these data in terms of energy, pitch angle, flux, and phase space density. Of specific applicability to this study, Looper has provided plots of the LET fluxes in units of $(cm^2\text{-sr-MeV})^{-1}$ for each of the LETs for energy intervals of 1.9–2.1 MeV, 2.1–2.9 MeV, 3.2–3.7 MeV, 3.7–4.3 MeV, and 4.3–5.0 MeV. These plots have been scanned to provide the high-energy proton database used in the study. Two examples of the scanned values are presented in Fig. 9, which compares them with Looper's Fig. 2.9. The red and blue dots are the scanned values overlaid on the Looper's LET C proton flux plots at 1.9–2.1 MeV (red) and 2.1–2.9 MeV (blue). It should be noted that the scanned values either overlay the actual points (the fits are in the middle of a vertical line which represents an error bar) or are located at the top of a line (the upper part of a vertical line). In the latter case, Looper has only plotted the upper limit on the measurement—this issue needs to be kept in mind when comparing the NMOD high-energy proton predictions as they may be biased towards an "upper limit".

6. Low-Energy Charged Particle Data Description

The other primary source of charged particle data from the Voyager flyby is the "Low-Energy Charged Particle" (LECP) instrument on Voyager 2. This instrument measured electrons with energies from 22 keV to greater than 1.2 MeV and protons (actually $Z \geq 1$ though in this study they will be assumed to be $Z = 1$) from 29 keV to 3.5 MeV. Observations by sector (e.g., pitch angle) and sector-averaged observations were provided to the PDS in the form of differential fluxes in units of $(n\#/cm^2\text{-s-sr-keV})$. Here the latter data (sector-averaged fluxes) averaged over 4-minute data intervals near closest approach (Day 24, Hours 13 to 22, 1986) for the channels given in Table 4 (adapted from Mauk et al., [1987] Table 1) form the basis of the NMOD analysis.

We note that there is an ambiguity in the PDS and published Neptune data as to whether the three highest electron channels were differential or integral. In previous studies (e.g., Uranus—Garrett et al., 2015) they were given as differential as indicated. Numeric checks demonstrated, as the spectra are relatively hard in this energy range, that there was ~10% or less error if differential fluxes were assumed instead of integral fluxes. As a consequence, it is assumed here that the PDS values were differential. In addition to the PDS data, Mauk et al. (1991, 1994, and 1995) have provided graphs of the raw electron and proton count-rate data for the period near closest approach to Neptune. Of particular value are the line plots in Fig. 9 of Mauk et al. (1991). These plots allowed a check of the corresponding PDS flux data. Their Figs. 8 and 9 provide plots of the raw count rate data that were scanned, digitized, and compared with the PDS data using the conversion factors in Table 4 above. Two sample plots overlaying the PDS, Mauk et al. (1987) count rate data, and Neptune radiation model predictions are provided in Figs. 10 and 11 of this document. The computed flux values from the scans agreed within a few percent of the PDS data validating the use of that data set for our modeling efforts. Expanding on this analysis, the PDS data at various energies for the electrons and protons are compared in later sections to the NMOD model predictions versus time, L-shell, and each other and are discussed in detail in that section.

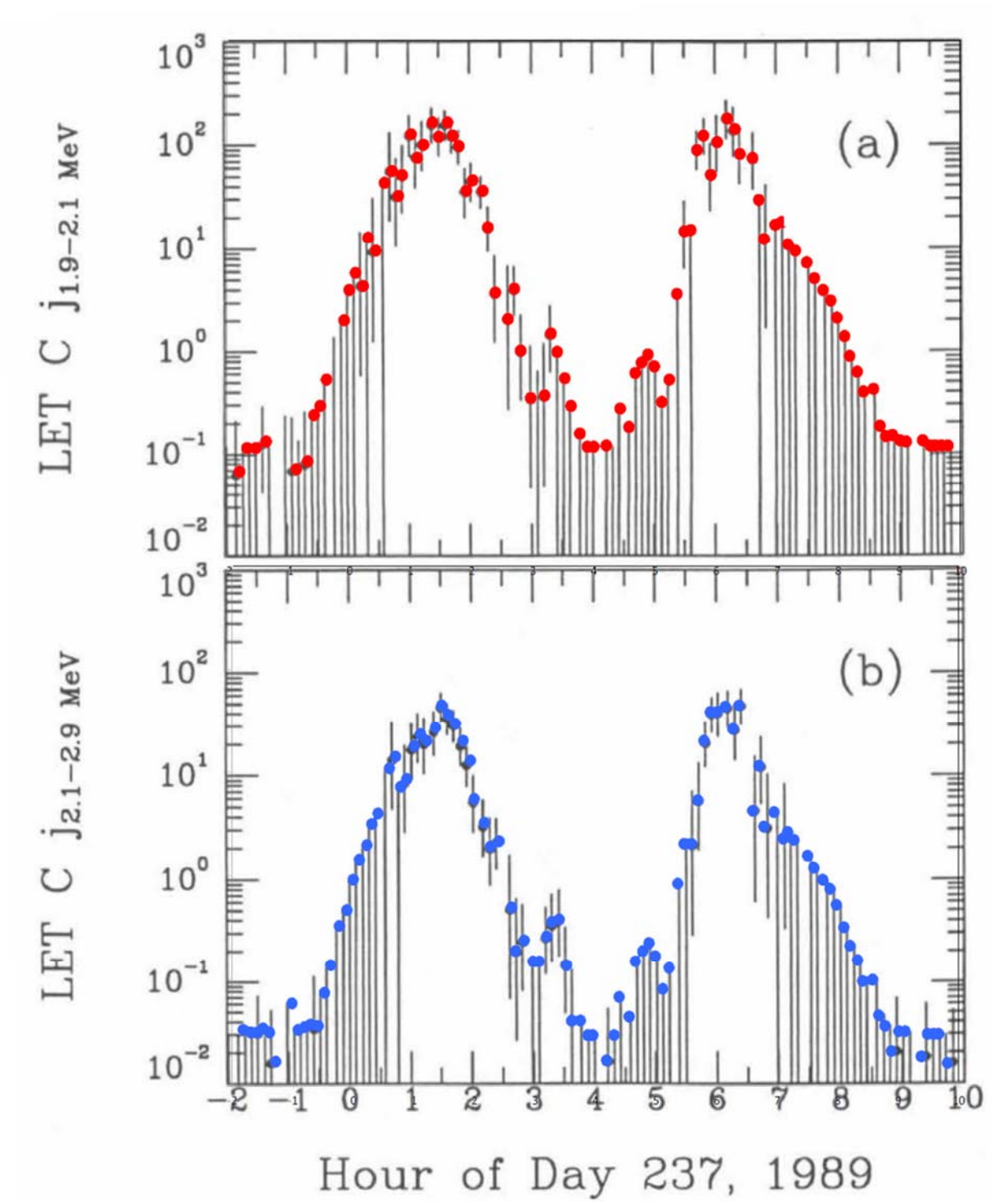

Figure 9. Representative scans of estimates of the CRS LET during the Voyager 2 flyby from Looper (1993). Note that the scanned values in red and blue (for the two energy ranges) are either on the points indicated or at the top of the error bars where no "median value" is indicated.

Table 4. Characteristics of the Voyager 2 LECP channels used in this study.

"Geo Mean Energy" is geometric mean energy (sqrt(E_{lo}*E_{hi})) for the channel. Channel characteristics are adapted from Mauk et al. [1987], Table 1.

Energies (MeV)	Geo Mean Energy (MeV)	dE (MeV)	ε GEO Factor*
e- 0.022-0.035	0.028	0.013	0.006
e- 0.035-0.061	0.046	0.026	0.006
e- 0.061-0.112	0.083	0.051	0.006
e- 0.112-0.183	0.143	0.071	0.0039
e- 0.183-0.5	0.302	0.317	0.002
e- 0.252-0.48	0.348	0.228	0.0081
e- 0.480-0.853	0.640	0.373	0.0035
e- 0.853-1.2	1.012	0.347	0.00017

Energies (MeV)	Geo Mean Energy (MeV)	dE (MeV)	ε GEO Factor
H^+ 0.028-0.043	0.035	0.015	0.113
H^+ 0.043-0.080	0.059	0.037	0.113
H^+ 0.08-0.137	0.105	0.057	0.113
H^+ 0.137-0.215	0.172	0.078	0.113
H^+ 0.215-0.54	0.341	0.325	0.113
H^+ 0.54-0.99	0.731	0.45	0.113
H^+ 0.99-2.14	1.456	1.15	0.113
H^+ 2.14-3.5	2.737	1.36	0.113

*Efficiency × geometric factor (units cm^2-sr)

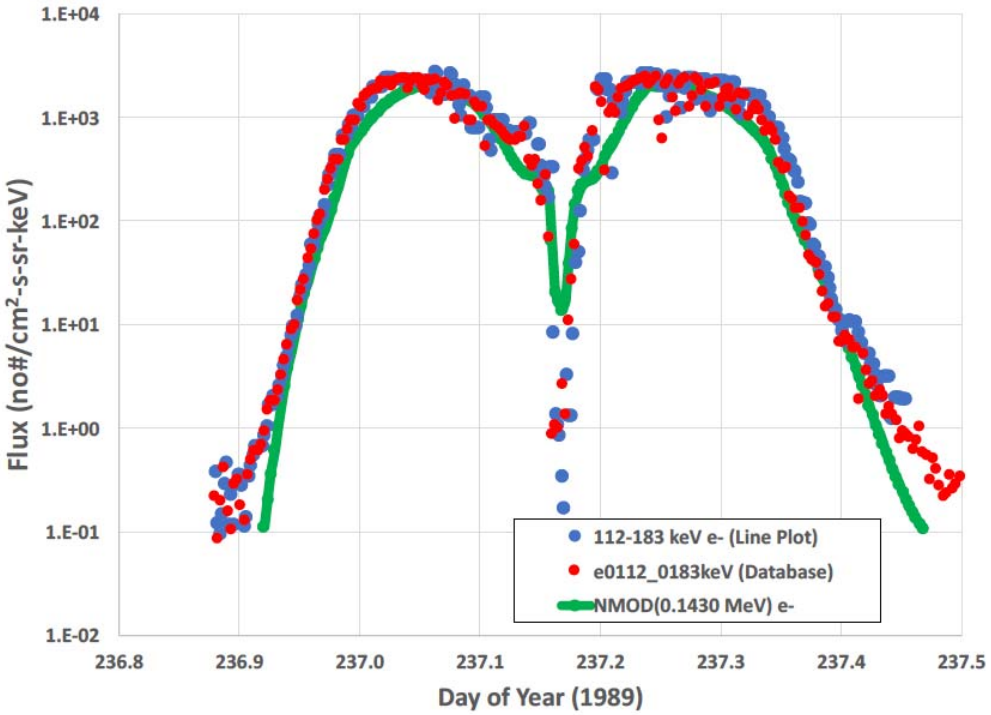

Figure 10. PDS electron flux data (red) versus spacecraft event time (SCET) during the encounter for the 112–183 keV channel compared with scanned count rate data (blue) from Mauk et al [1991], Fig. 9, converted to fluxes using Table 4 above. NMOD model fluxes are shown in green.

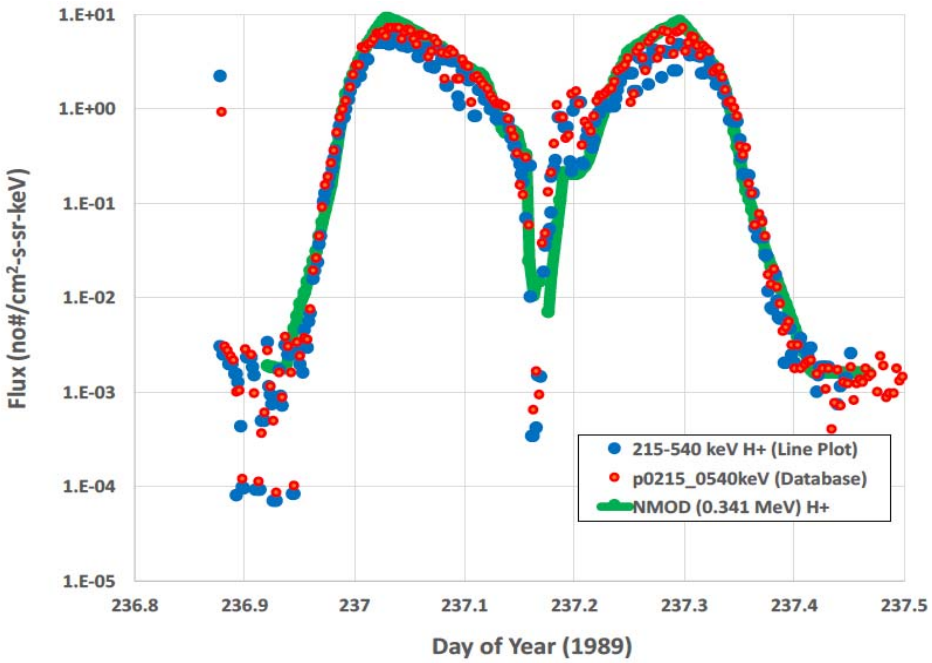

Figure 11. PDS proton flux data (red) versus SCET during encounter for the 215–540 keV channel compared with scanned count rate data (blue) from Mauk et al. [1991], Fig. 9, converted to fluxes (Table 4 above). The NMOD model fluxes are shown in green.

Given the LECP particle data, the O_8 and OTD magnetic field components were then computed for the flyby for each 4-minute average interval. Figures 12 and 13 compare the PDS flux data with the NMOD model predictions for L-shell variations. Note that there are different branches in the region 5–10 L. The reason for this is that data in this L range were taken at very different magnetic latitudes. As will be discussed in the next section, comparing these differences allows a determination of the pitch angle distributions along the L-shell. The PDS data are of particular importance because they will be used to validate the NMOD radiation model by comparing the predictions of the model to the actual fluxes as illustrated in these figures.

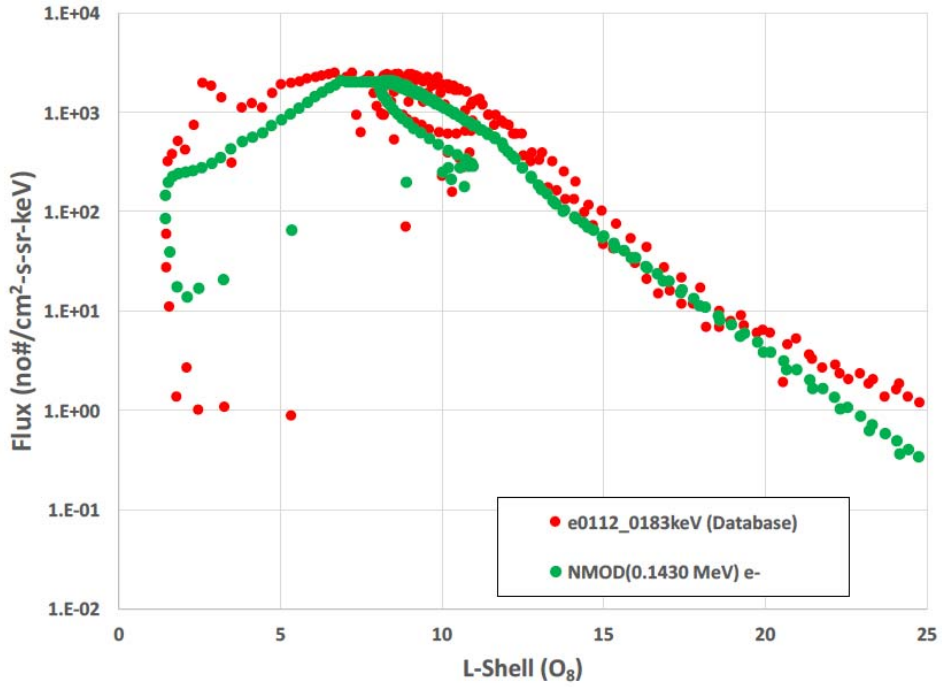

Figure 12. Electron flux data versus L-shell (O_8) from the PDS (red) for the 112–183 keV channel compared with the NMOD fluxes (green).

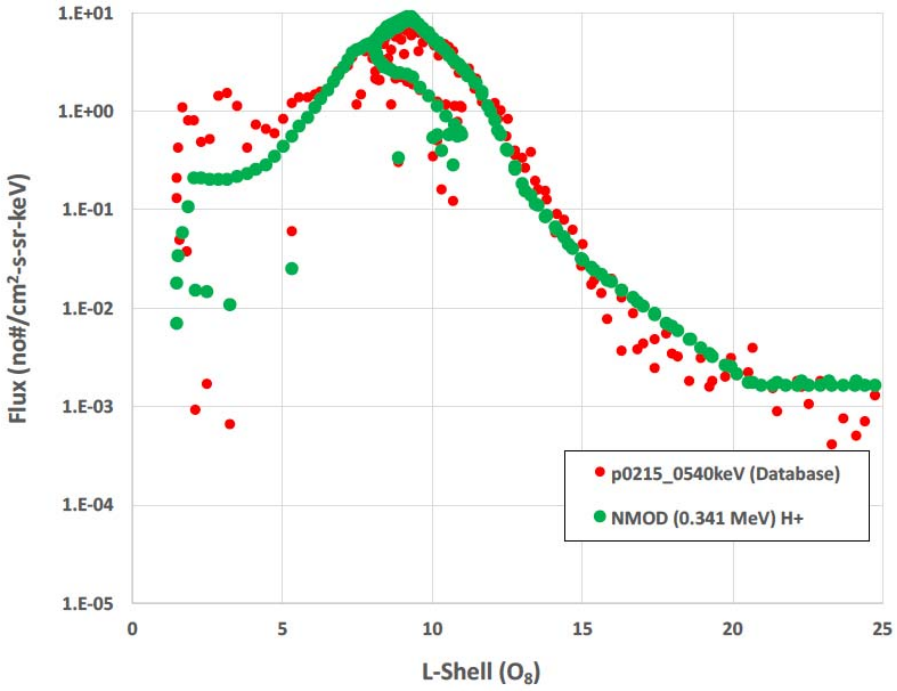

Figure 13. Proton flux data (red) versus L-shell (O_8) from the PDS for the 215–540 keV channel compared with the NMOD fluxes (green).

7. Analysis of the Differential Flux Intensity Spectra

As the first step in developing a model capable of predicting the Neptunian electron and proton fluxes, selected (published and PDS data) particle spectra were fit in terms of energy and L-shell/SCET. These spectra form the core of the NMOD model to be presented here. Selesnick and Stone [1992], for example, published several integral electron and proton spectra. One of these spectra for the CRS TET was converted to a differential flux spectrum and is presented in Fig. 14 for Day 237 at 01:38 UT. Also plotted is the corresponding estimate of the CRS TET electron flux at this time based on the Stone et al. [1989] spectral fits discussed earlier (e.g., the power law fits in Table 3). Similarly, LECP electron and proton differential spectra plots are available at specific locations and as high-resolution data in the PDS. An example of the corresponding LECP electron PDS data for Day 237 at 01:38 UT are plotted in Fig. 14. The differential spectrum fit (the orange curve in Fig. 14) was developed using a standard regression technique in Excel to fit an equation of the form:

$$Log_{10}(f'(E)) = A_0 + A_1(Log_{10}(E))^1 + A_2(Log_{10}(E))^2 + A_3(Log_{10}(E))^3 + A_4(Log_{10}(E))^4 + A_5(Log_{10}(E))^5 \quad (4)$$

Where:

E = Energy (keV)

f' = Predicted differential intensity spectrum at energy E and SCET time t (units are $(cm^2\text{-s-sr-keV})^{-1}$)

A_i = Regression fit constants where i = 0, 1, 2, 3, 4, 5 for electrons [corresponding to (E0, E1, E2, E3, E4, E5) for electrons and (P0, P1, P2, P3, P4, P5) for protons in Table 6]

Table 5 lists the times and locations of the spectra used in developing the model. The constants and the regression coefficient, R^2, for each fit to these spectra are listed in Table 6. The complete set of spectra from Mauk et al. [1987] or the PDS used in the model and of the fits to the differential electron and proton spectra are provided in Appendix A1. Note that these spectral fits represent the basis of the NMOD model with the exception of corrections for pitch angle variations for locations off the magnetic equator. These corrections are discussed in the next section. Fluxes at locations at L-shell values between those listed are to be estimated by linearly interpolating the Log_{10} of the fluxes in L between the adjacent points.

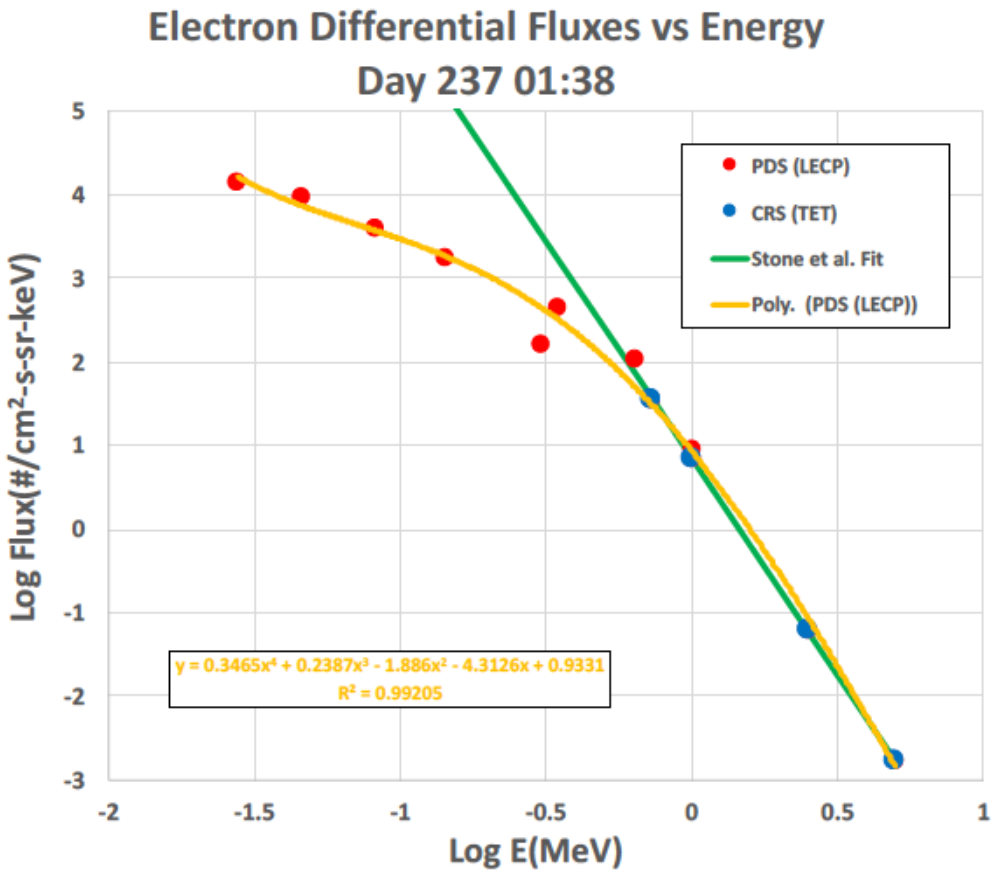

Figure 14. In-situ electron data compared with NMOD fits for Day 237 01:38 SCET. Blue symbols are differential intensities versus energy from TET pulse height analyzer (Fig. 5 from Selesnick and Stone [1992]) at Neptune. Red symbols correspond to PDS LECP measurements at the same time. The orange curve is a smoothed fit to data points—the green line is power law fit from Stone et al. [1989] for ~0.5-1 MeV. See Appendix A1 for more examples.

Table 5. Average SCET, radial distance (R_n), latitude (degrees), west longitude (degrees+12°), magnetic field (O_8) at the spacecraft (B_{sc}) and the equator (B_{eq}), and the L-shell (O_8) for the spectra used in this study.

A) Neptune Electron Spectra Locations:

DOY(1989)	Range	Latitude	W_{long}+12°	B_{sc}	B_{eq}	L (O_8)
237.1903	2.352	18.194	274.750	1.926E-02	1.580E-02	2.08
237.2056	3.339	5.936	285.770	7.234E-03	2.894E-03	3.67
237.2181	4.159	0.328	293.710	3.728E-03	1.135E-03	5.04
237.2292	4.885	-3.191	300.440	2.149E-03	6.199E-04	6.09
237.2403	5.608	-5.766	306.970	1.325E-03	4.225E-04	6.89
237.2458	5.968	-6.812	310.180	1.062E-03	3.672E-04	7.22
237.0681	6.833	-13.939	30.257	4.892E-04	2.482E-04	8.20
237.3389	11.864	-15.058	1.964	8.627E-05	8.517E-05	11.76
236.9792	12.441	-20.503	341.000	8.524E-05	6.170E-05	13.11
236.9750	12.700	-20.668	338.730	8.200E-05	5.515E-05	13.61
237.5097	22.349	-19.059	94.542	1.588E-05	6.904E-06	27.30

B) Neptune Proton Spectra Locations:

DOY(1989)	Range	Latitude	W_{long}+12°	B_{sc}	B_{eq}	L (O_8)
237.1736	1.423	50.667	253.787	8.514E-02	3.315E-02	1.63
237.1903	2.353	18.351	274.707	1.959E-02	1.632E-02	2.09
237.0089	3.795	2.498	290.253	4.915E-03	1.619E-03	4.45
237.0104	6.147	-7.281	311.770	9.586E-04	3.462E-04	7.37
237.0112	7.397	-9.979	322.807	4.827E-04	2.478E-04	8.23
237.2958	9.162	-12.563	338.290	2.131E-04	1.703E-04	9.32
237.3361	11.691	-14.929	180.442	9.042E-05	8.979E-05	11.56
236.9792	12.441	-20.502	341.003	8.529E-05	6.177E-05	13.11
237.0156	14.020	-16.370	20.896	5.501E-05	4.127E-05	15.02
236.9375	15.021	-21.903	318.300	6.154E-05	1.586E-05	20.71
237.5444	24.458	-19.504	113.275	1.042E-05	6.901E-06	27.29
237.4764	20.325	-18.641	76.564	2.093E-05	6.774E-06	27.48

Table 6. Regression fit constants and coefficients defined in Eq. 4 for the differential intensity spectra in Appendix A1. E0–E5 are the electron constants while P0–P5 are the proton constants. Units are $(cm^2\text{-}s\text{-}sr\text{-}keV)^{-1}$.

A) Neptune Electron Spectra Locations:

DOY(1989)	L Shell	E0	E1	E2	E3	E4	E5	R^2
237.1903	2.08	-0.4361	-4.8752	-1.5102	0	0	0	0.99014
237.2056	3.67	0.6619	-4.0370	-2.0470	-0.4076	0	0	0.99794
237.2181	5.04	0.2544	-4.8457	-1.9658	-0.2111	0	0	0.99381
237.2292	6.09	1.0671	-3.9595	-1.9116	-0.3898	0	0	0.98701
237.2403	6.89	1.2638	-3.8113	-1.7184	-0.2691	0	0	0.97916
237.2458	7.22	1.2028	-3.8459	-1.6927	-0.2597	0	0	0.97873
237.0681	8.20	1.0131	-4.1861	-1.8681	-0.2873	0	0	0.98127
237.3389	11.76	-0.7289	-5.2139	-1.2791	0	0	0	0.99673
236.9792	13.11	-1.6575	-4.8516	0.2140	0.5742	0	0	0.99517
237.9750	13.61	-2.0601	-4.8676	0.6840	0.7764	0	0	0.98743
237.5097	27.30	-4.9843	-4.4922	0.4114	0	0	0	0.99102

B) Neptune Proton Spectra Locations

DOY(1989)	L Shell	P0	P1	P2	P3	P4	P5	R^2
237.1736	1.63	-3.0586	-2.9017	0.4611	0	0	0	0.97756
237.1903	2.09	-3.3629	-4.3622	6.0699	2.0776	-6.5009	-3.2785	0.99237
237.0089	4.45	-3.0972	-4.2345	5.1296	1.7893	-5.579	-2.7871	0.99606
237.0104	7.37	-0.1901	-2.4162	-1.6982	-1.3367	0.505	0.6220	0.97238
237.0112	8.23	-0.1521	-2.2822	-0.9049	-1.7686	-1.0167	0	0.95753
237.2958	9.32	-0.3786	-3.6792	-1.9184	-1.2677	-0.5913	0	0.98539
237.3361	11.56	-1.6307	-4.5747	-0.2706	1.3777	0.3143	0	0.99864
236.9792	13.11	-3.1592	-3.7497	4.5387	1.7385	-4.8754	-2.4809	0.99399
237.0156	15.02	-3.7278	-3.1696	4.9338	1.399	-4.9651	-2.3854	0.99232
236.9375	20.71	-4.1131	-1.4917	2.9615	-0.4205	-2.3931	-0.8724	0.99263
237.5444	27.29	-3.7942	-1.5240	-0.109	-1.5437	-0.5659	0	0.99858
237.4764	27.48	-3.7624	-1.2557	0.6236	-1.1312	-0.4761	0	0.99966

8. Pitch Angle Distributions

As illustrated in Figs. 12 and 13, there can be large differences between Voyager 2 measurements at the same L-shell positions. The reason for these differences is believed to be in large part due to pitch angle variations. As discussed in Selesnick and Stone (1991), to first order, the pitch angle variations can be described in terms of Eq. 1 where the pitch angle variations are assumed to be proportional to $sin^{2n}(\alpha)$ where n is a "to be determined" fit parameter and α is the magnetic pitch angle of the particle relative to the magnetic field vector at the specified location. Mauk et al. [1991] have provided snapshots (their Fig. 8) of the normalized pitch angle variations along the Voyager 2 trajectory at 25 locations for the electrons and 22 for the ions. The snapshots were for the 28–43 keV and 137–215 keV ions (assumed here to be protons) and for the 22–35 keV and >252 keV electrons. A standard regression technique was used to fit the normalized plots in terms of $sin^{2n}(\alpha)$. Table 7 lists the regression fit coefficients. The original LECP data and the regression fit predictions for $2n$ are plotted in Fig. 15. Figure 16 illustrates the final fits to the $2n$ values presented in Table 7. The two fit equations are as follows (note: the fits are both to the "lo" and "hi" energy ranges simultaneously):

$$2n_e = -0.0004\,L^3 + 0.0273\,L^2 - 0.5514\,L + 3.6712 \quad (5)$$

$$2n_p = 0.0049\,L^2 - 0.2568\,L + 2.913 \quad (6)$$

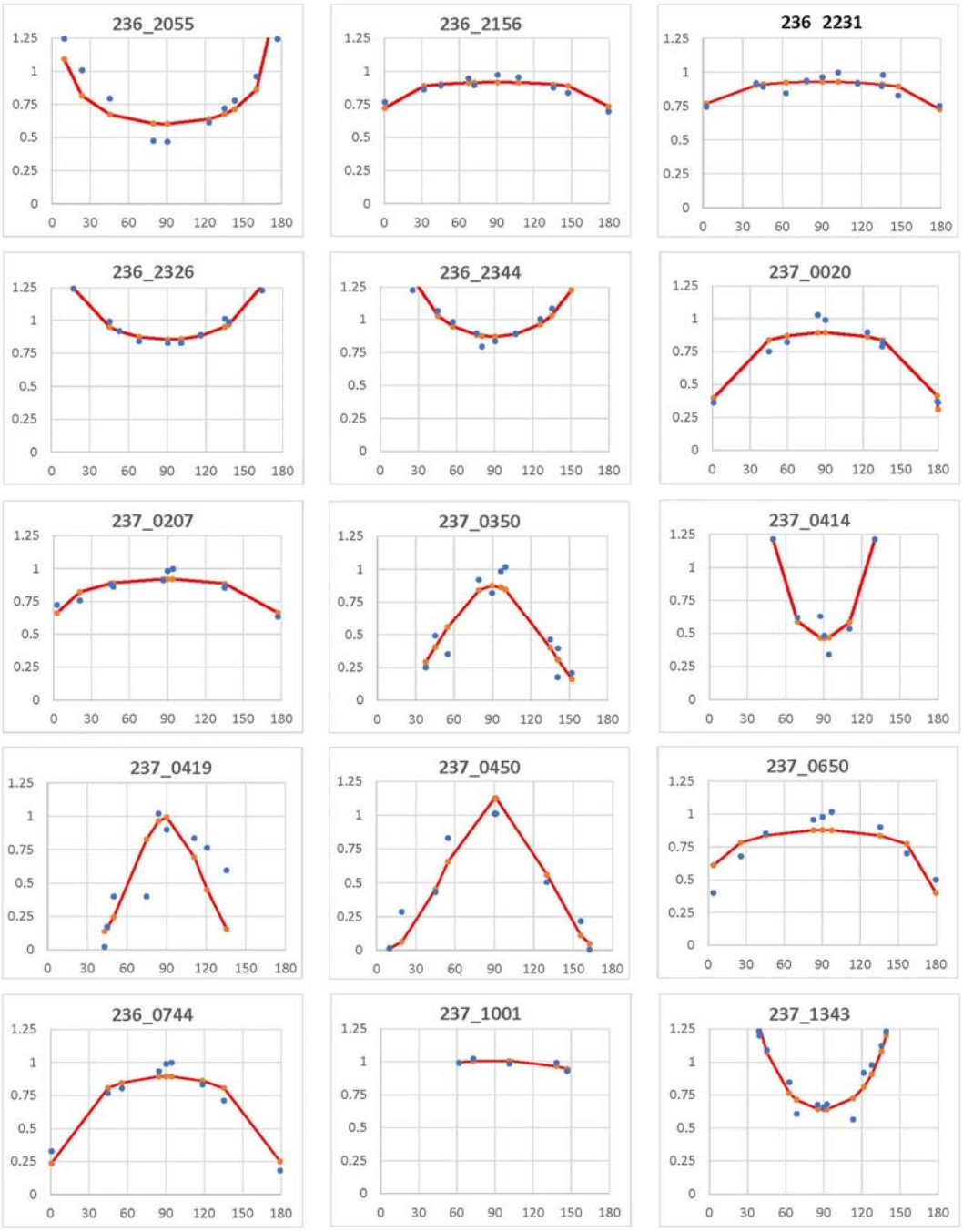

A) Electrons 22–35 keV

Figure 15. Fits to the LECP pitch angle variations (based on Mauk et al. [1991] Fig. 8). The fit constants determined by linear regression are presented in Table 7. Parameters represented are A) electrons 22–35 keV, B) electrons > 252 keV, C) ions 28–43 keV, and D) ions 137–215 keV.

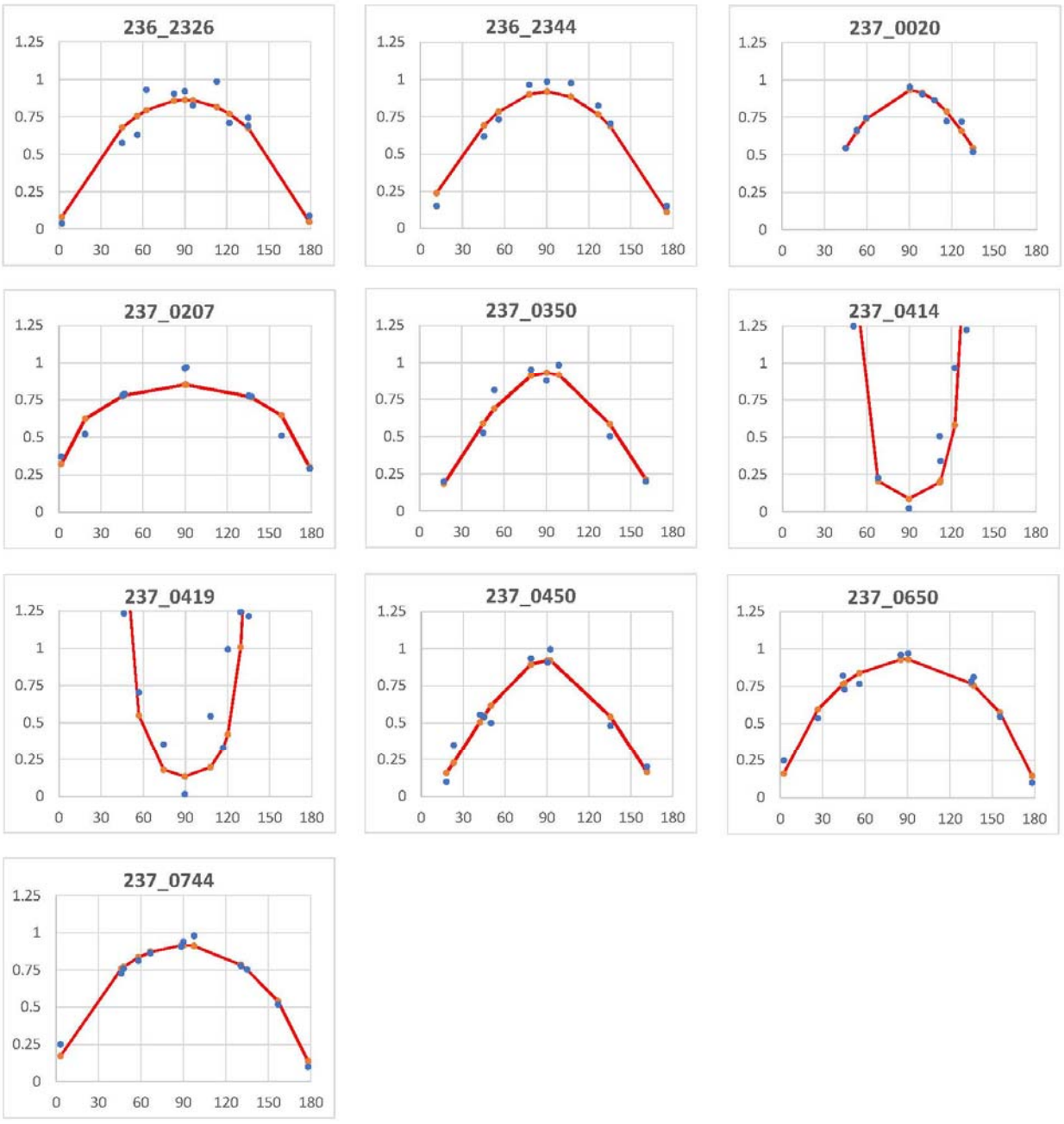

B) Electrons >252 keV:

Figure 15 (cont.). Fits to the LECP pitch angle variations (based on Mauk et al. [1991] Fig. 8). The fit constants determined by linear regression are presented in Table 7. Parameters represented are A) electrons 22–35 keV, B) electrons > 252 keV, C) ions 28–43 keV, and D) ions 137–215 keV.

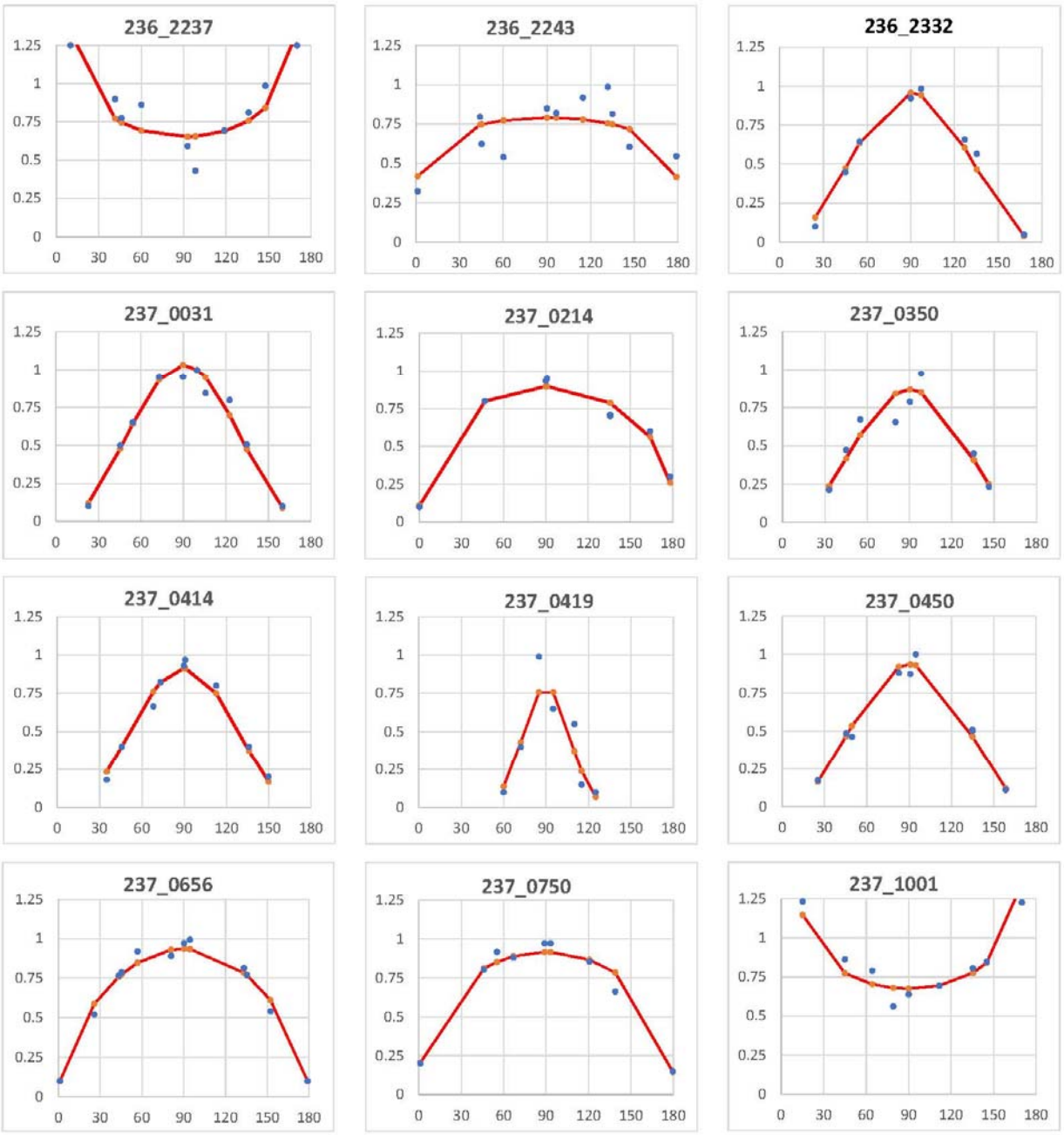

C) **Ions 28-43 keV**

Figure 15 (cont.). Fits to the LECP pitch angle variations (based on Mauk et al. [1991] Fig. 8). The fit constants determined by linear regression are presented in Table 7. Parameters represented are A) electrons 22–35 keV, B) electrons > 252 keV, C) ions 28–43 keV, and D) ions 137–215 keV.

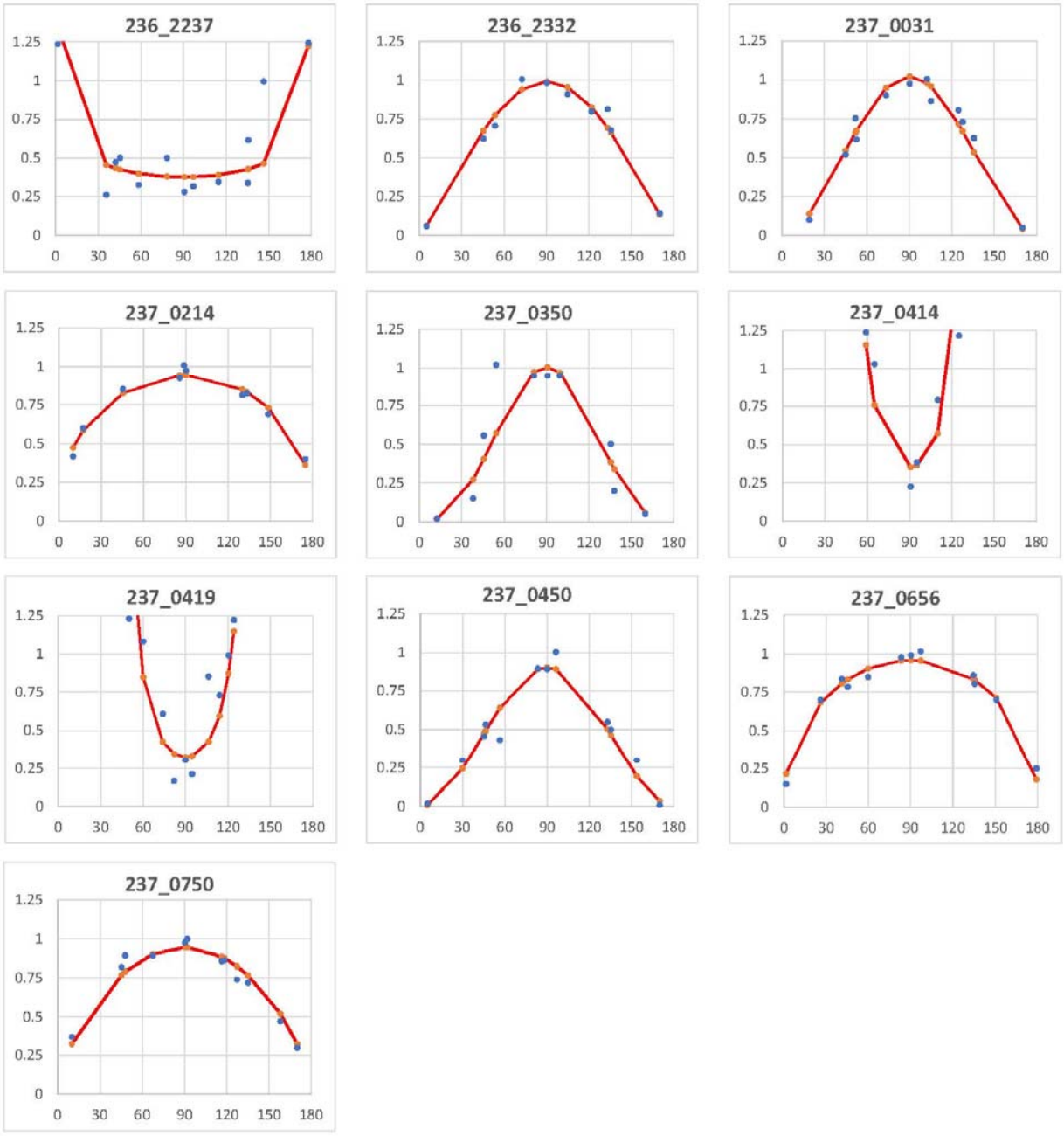

D) Ions 137–215 keV

Figure 15(cont.). Fits to the LECP pitch angle variations (based on Mauk et al. [1991] Fig. 8). The fit constants determined by linear regression are presented in Table 7. Parameters represented are A) electrons 22–35 keV, B) electrons > 252 keV, C) ions 28–43 keV, and D) ions 137–215 keV.

The pitch angle plots in Fig. 15 and their fits indicate that some of the distributions are field aligned as opposed to being trapped. This is indicated numerically by a negative value for *2n* in Table 7A. This does not present a problem for integration of directional flux over pitch angle

(see next paragraph) but it does in spirit at least violate the concept of "trapped radiation". Some of these fitted values are a lot greater than ~2–3. While these values may be real, they primarily occur in a narrow region near the planet when values are changing extremely rapidly and would skew any fit to the majority of the data. It was decided therefore to restrict the "*2n*" fits presented in Fig. 16 to the L-shell range 3–30 L. The limits this poses on the model will be discussed later.

Table 7. Regression fits to $A_0\ sin^{2n}(\alpha)$ for Fig. 15. As the pitch angle curves were normalized prior to fitting, A_0 should ideally be ~1 for all fits.

A) Fits to the pitch angle plots in Fig. 15: "2n"

UT	L	Electrons 22–35 keV	Electrons >252 keV	Ions 28–43 keV	Ions 137–215 keV
237_0419	1.52	5.2331	-7.8313	12.1690	-6.6520
237_0414	1.52	-3.5948	-11.2102	2.4645	-7.7781
237_0450	3.20	2.6243	1.4992	2.0387	1.8687
237_0350	5.85	2.2451	1.3417	2.1169	2.6985
237_0207	8.16	0.1077	0.2734		
237_0214	8.22			0.3606	0.3900
237_0650	8.87	0.1367	0.5517		
237_0656	9.03			0.5575	0.4126
237_0031	9.65			2.2683	1.8141
237_0020	10.12	0.1909	1.5492		
237_0744	10.64	0.2951	0.5659		
237_0750	10.90			0.3712	0.6105
236_2344	12.07	-0.4880	0.8334		
236_2332	12.95			2.0349	1.1359
236_2326	13.44	-0.3087	0.7041		
236_2243	18.30			0.1593	
236_2237	19.61			-0.4084	-0.3504
236_2231	20.33	0.0615			
237_1001	20.77	0.1076		-0.3940	
237_1343	27.07	-1.4901			
236_2156	29.37	0.0481			

Table 7. (Continued)

B) Fits to the pitch angle plots in Fig. 15: "Ao".

UT	L	Electrons 22–35 keV	Electrons >252 keV	Ions 28–43 keV	Ions 137–215 keV
237_0419	1.52	0.99	0.14	0.79	0.33
237_0414	1.52	0.46	0.09	0.91	0.35
237_0450	3.20	1.13	0.92	0.94	0.90
237_0350	5.85	0.87	0.93	0.87	1.00
237_0207	8.16	0.92	0.85		
237_0214	8.22			0.89	0.94
237_0650	8.87	0.88	0.93		
237_0656	9.03			0.94	0.96
237_0031	9.65			1.03	1.02
237_0020	10.12	0.89	0.93		
237_0744	10.64	0.89	0.92		
237_0750	10.90			0.92	0.95
236_2344	12.07	0.87	0.92		
236_2332	12.95			0.96	0.99
236_2326	13.44	0.85	0.86		
236_2243	18.30			0.79	
236_2237	19.61			0.65	0.38
236_2231	20.33	0.93			
237_1001	20.77	1.01		0.68	
237_1343	27.07	0.64			
236_2156	29.37	0.92			

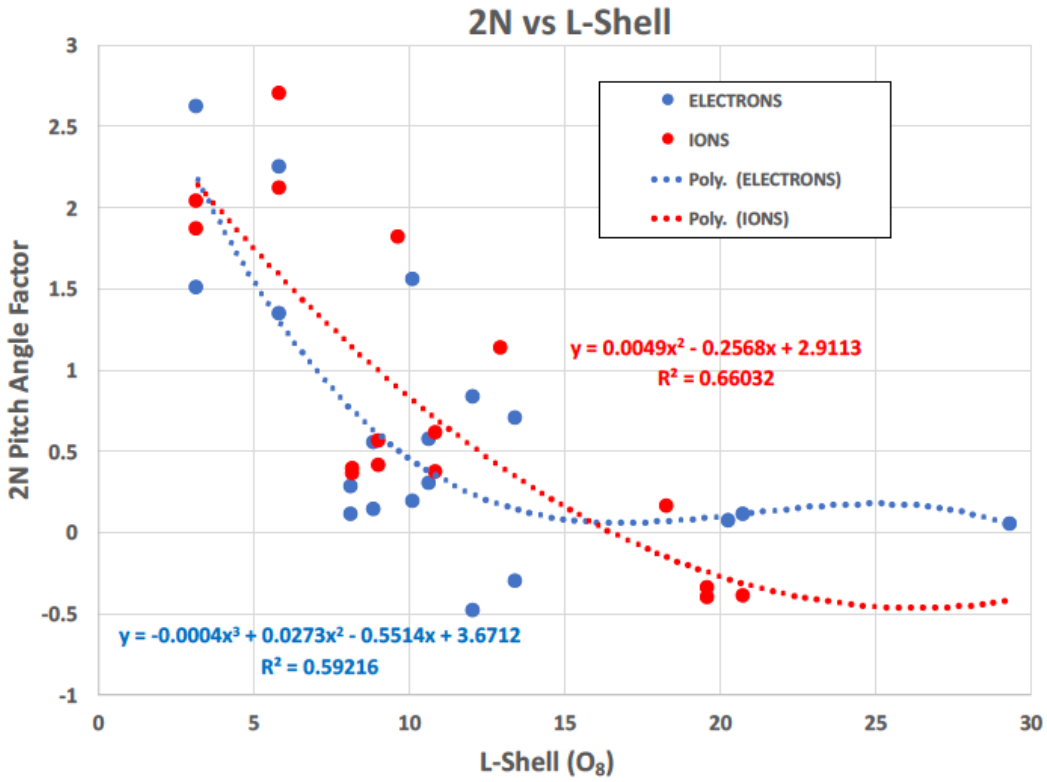

Figure 16. Fits to the "2*n*" values presented in Table 7 and based on the Mauk et al. [1987] pitch angle distributions of Fig. 15. The fits are to both the "lo" and "hi" energy ranges for each species simultaneously.

The normalized pitch angle function multiplied by the sector averaged differential spectrum provides a complete definition of the particle distribution at the given observation location. To determine the differential "omnidirectional" intensity at a point, one integrates that function over pitch angle. To be specific, NMOD uses the pitch angle distributions as presented above to compute the omnidirectional flux, which is typically used by the radiation shielding community to model dosage. That is the following equation is integrated numerically over the pitch angle assuming a functional form of "$sin^{2n}(a)$":

$$J(E) = \int_{-\pi}^{\pi} d\alpha \int_{0}^{2\pi} j(E,\alpha)\, sin(\alpha)\, d\phi = 4\pi \int_{0}^{\pi} [f'(E) sin^{2n}(\alpha)] sin\,(\alpha) d\alpha \qquad (7)$$

where:

$J(E)$ = omnidirectional differential flux versus energy E; units are $(cm^2\text{-s-keV})^{-1}$

$j(E,\alpha)$ = angular differential flux versus energy E; assumed to be given by: $f'(E)\ \sin^{2n}(\alpha)$; units are $(cm^2\text{-s-sr-keV})^{-1}$

ϕ = angle normal to the magnetic field

α = pitch angle at location of spacecraft/observation

$f'(E)$ = measured particle differential intensity given by plots in Appendix A1 and Eq. 4 and averaged over the LECP sectors (Fig. 16, Table 7)

The units derived above are in $(cm^2\text{-s-keV})^{-1}$ for the "omnidirectional fluxes." As the spectra in Appendix A1 are assumed to be averaged over the LECP sectors, dividing the omnidirectional flux by 4π gives the proton and electron differential intensity spectra. This averaged "differential intensity" or equivalently the omnidirectional value is what is normally provided to the radiation shielding modelers. That is:

$$I(E) = J(E)/4\pi \tag{8}$$

where:

$I(E)$ = sector averaged differential intensity spectra, units are now $(cm^2\text{-s-sr-keV})^{-1}$

Up to this point in the discussion, the particle fluxes are computed at the location of the spacecraft/observation and, since the pitch angle distributions are normalized at that location, should simply reproduce the spectra in Appendix A1. To make the NMOD radiation model useful for all locations along a field line, however, the differential intensity spectrum f'_α needs to be transformed to the magnetic equator from the spacecraft location and the integration carried out over α_0 as opposed to α. To do this, Eqs. 2 and 3 need to be inverted to give the relevant variables in terms of the more general equatorial values:

$$\alpha_0 = sin^{-1}\left(\left(\frac{B_0}{B}\right)^{1/2}\sin(\alpha)\right) \tag{9}$$

$$f'_{\alpha_0}(E) = f'_\alpha(E)\left(\frac{B}{B_0}\right)^n \tag{10}$$

where:

f'_{α_0} = differential intensity at the equator

f'_α = differential intensity at the spacecraft

The "n" values (Eqs. 5 and 6) along with B at the spacecraft and B_0 (B at the equator) for the L-shell are then used to compute the "correction" factor, $(B/B_0)^n$, to f'_α to give f'_{α_0} at the magnetic equator. Estimates of 2n, the ratio (B/B_0), and $(B/B_0)^n$ are listed in Table 8. The latter correction factor is plotted versus L in Fig. 17. Values are provided at L-shell values corresponding to the model spectra in Tables 5 and 6. The correction is then applied to each spectrum (note: this implicitly assumes that the pitch angle distribution measured at the spacecraft is equal to that at the magnetic equator and that the correction applies over the entire energy range).

To summarize, the differential intensity and pitch angle distributions at the spacecraft location are transformed to the magnetic equator at the L-shell position for that observation. For an arbitrary location along the field line, the equatorial spectrum is then integrated over pitch angle. The limits on that integration are defined to be between the 90° pitch angle at the desired location (given by substituting 90° into Eq. 7) and the critical pitch angle for atmospheric absorption—the pitch angle at which a particle will be lost to the atmosphere. This angle, α_c, at the equator is computed by substituting $\alpha = 90°$ and $B = B_c$ in Eq. 9 where B_c is the value of the

magnetic field at the top of the atmosphere on the field line. B_c is given by the following fit to the surface magnetic field at Neptune:

$$Log_{10}(B_c) = - 0.1945\ L^6 + 1.641\ L^5 - 5.6092\ L^4 + 9.9491\ L^3 - 9.7534\ L^2 + 5.2173 - 1.8768 \quad (11)$$

where:

B_c = minimum magnetic field strength at top of atmosphere for specified magnetic L-shell passing through desired location for O_8 magnetic field model.

Table 8. Equator fit values with protons on the left and electrons on the right.

L	Ratio (B_{SC}/B_{EQ})	2n	Ratio^n
1.63	2.568	2.505	3.259
2.09	1.200	2.397	1.244
4.45	3.036	1.865	2.816
7.37	2.769	1.285	1.924
8.23	1.948	1.130	1.458
9.32	1.251	0.943	1.112
11.56	1.007	0.598	1.002
13.11	1.381	0.387	1.064
15.02	1.333	0.160	1.023
20.71	3.881	-0.306	0.813
27.29	1.509	-0.447	0.912
27.48	3.089	-0.445	0.778

L	Ratio (B_{SC}/B_{EQ})	2n	Ratio^n
2.08	1.22	2.641	1.299
3.67	2.50	1.997	2.496
5.04	3.29	1.534	2.489
6.09	3.47	1.236	2.156
6.89	3.14	1.036	1.808
7.22	2.89	0.962	1.667
8.20	1.97	0.765	1.296
11.76	1.01	0.312	1.002
13.11	1.38	0.233	1.038
13.61	1.49	0.215	1.044
27.30	2.30	0.826	1.410

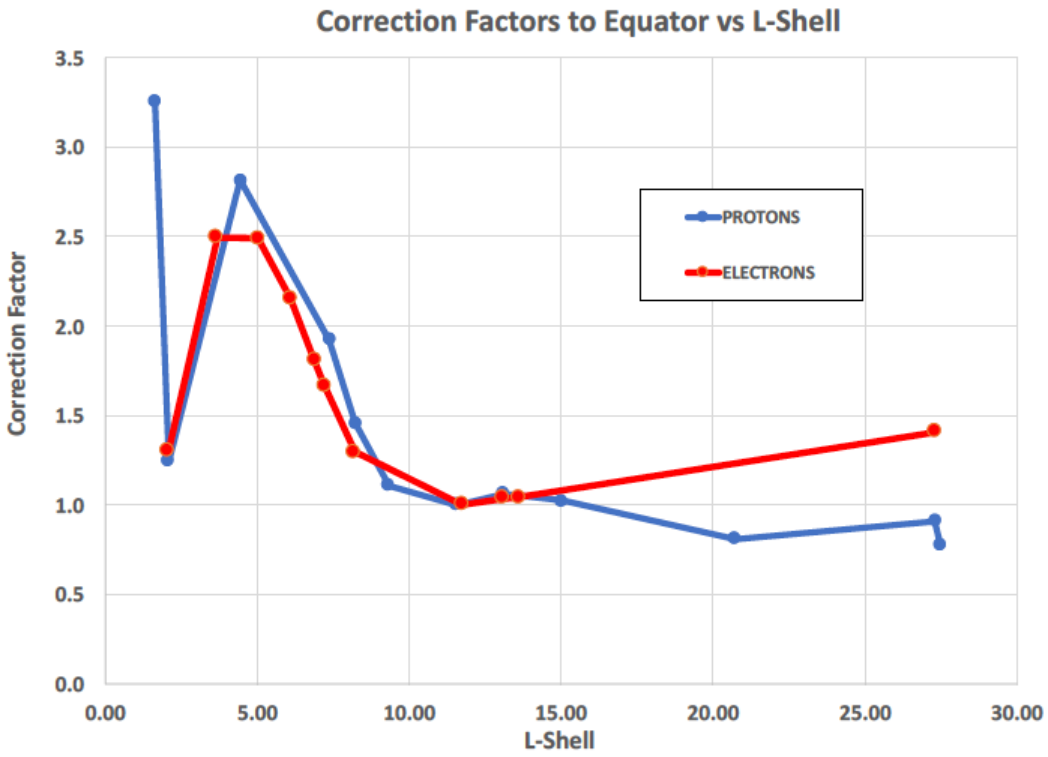

Figure 17. Estimates of the correction factor $(B/B_0)^n$ at the magnetic equator as defined by Eq. 10. Values are as listed in Table 8 at selected L values corresponding to the model spectra in Tables 5 and 6. The red curve is for electrons, the blue for protons.

9. NMOD Radiation Model

The preceding section has defined the primary elements of the NMOD Neptunian radiation model. The steps, in order, to carry out the computation of the omnidirectional differential intensity are as follows (Mauk et al., 1991, 1994, 1995; Stone et al., 1989; Connerney et al., 1991; Looper, 1993):

1. Define the L-shell, B(location), and B_{eq} as defined by the O_8 magnetic field model of Connerney et al. (1991) for two L-shells for which spectra exist and that bracket the L-shell passing through the desired location.
2. Compute the spectra versus energy for the protons and electrons as defined by Mauk et al. (1991, 1994, 1995), Stone et al. (1989), and Looper (1993) at the magnetic equator (that is, apply the equatorial correction factor to the original fitted spectra) for the two bracketing L-shell values.
3. Similarly, define the normalized pitch angle variations for the electrons and protons at the magnetic equator for both L-shells.
4. Integrate the resulting spectra at the two locations over pitch angle between the specified mirror point angle and B_c at the equator.
5. Linearly interpolate the Log_{10} of the differential intensity between the two bracketing estimates to give the value at the location and at the selected energy.

6. If the integral flux is desired, repeat at higher energies and numerically integrate to approximate the integral.

A compiled version of the NMOD program that accomplishes these steps has been developed (see JPL IOM 5130-17-007 [Garrett and Evans, 2017] appendices for a complete listing). The model results are compared with the PDS data in Figs. 18–21 as functions of SCET and L-shell for the Voyager 2 flyby on August 24–25, 1989. The figures show that the NMOD model appears to provide an adequate fit to the electron data over much of the time and L-shell ranges. While over most of the energy range the proton data also appear to fit the PDS data, the three highest energy channels deviate from the PDS data by large factors near closest approach. This behavior can also be seen in some of the proton spectra fits in Fig. A1-2 where the scatter in the highest energy channel data for several of the spectra at these energies are quite large (we believe this is because of our assumption of the "highest values" for the proton fluxes when no mid-point was indicated in Looper's data plots—see earlier discussion). The L-shell plots for the protons, similar to the electron plots, agree well except inside ~3 L where there is again a large scatter in the data as there are very rapid changes in L and magnetic latitude during closest approach. Again, the disagreement is primarily in the three highest energy channels with them being overestimated during closest approach when the spacecraft was well above the magnetic equator. Clearly, further adjustments in the model are required between 1.5 and 3 L in the equatorial correction factor and probably in the pitch angle variations to account for these differences. Even so, the model fits the proton data reasonably well outside 3 L as currently formulated.

Figures 22 and 23 complete the comparisons between the PDS and NMOD by carrying out a cross-correlation analysis between the Log_{10} of the fluxes by energy channel for the in-situ data and the model estimates. The correlation coefficients (and fit formulas) versus energy channel are tabulated in Tables 9 and 10.

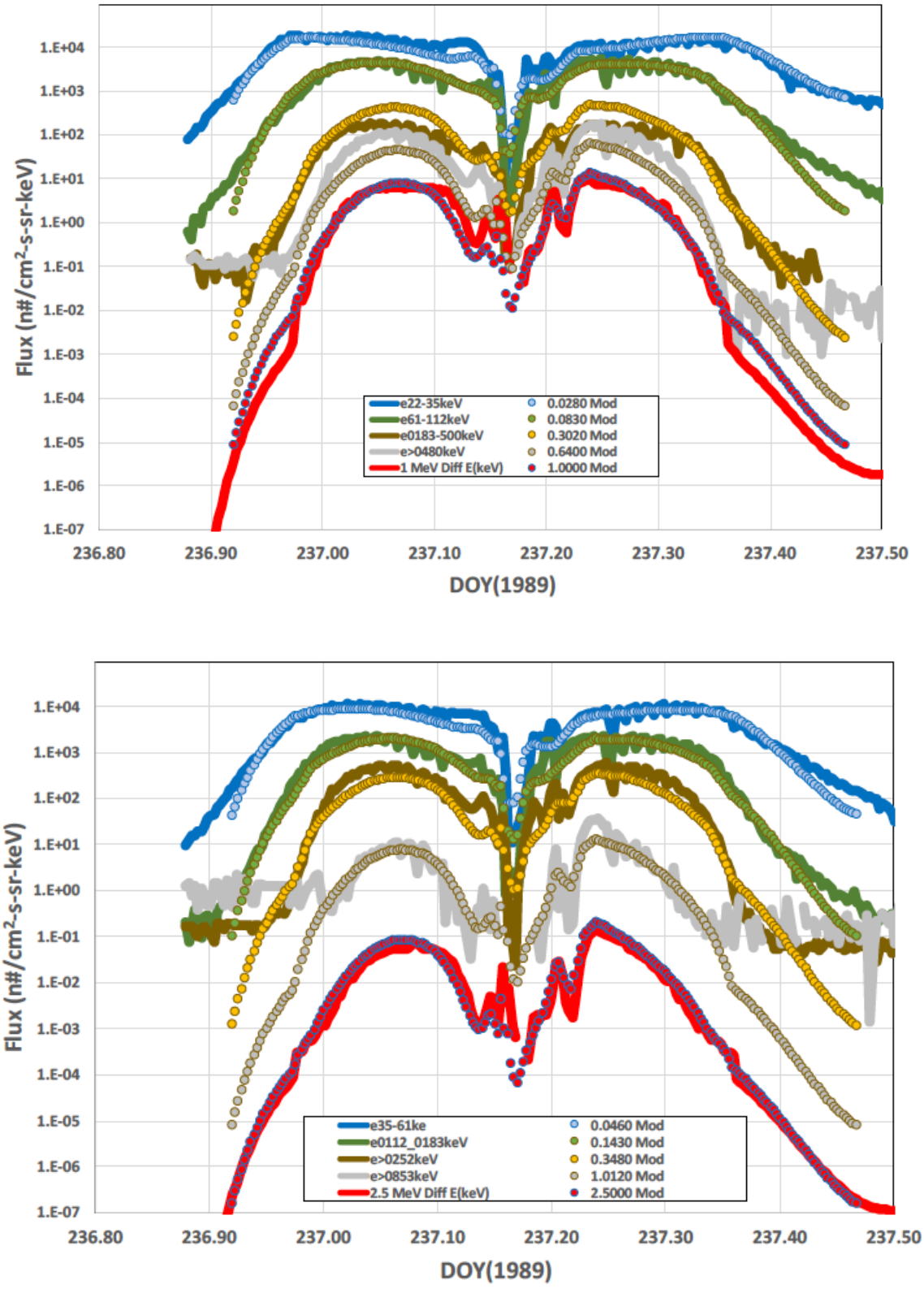

Figure 18. Electron flux data versus time from the PDS for the specified energies compared with the corresponding NMOD model fluxes. The top and bottom charts show alternating energy ranges for clarity.

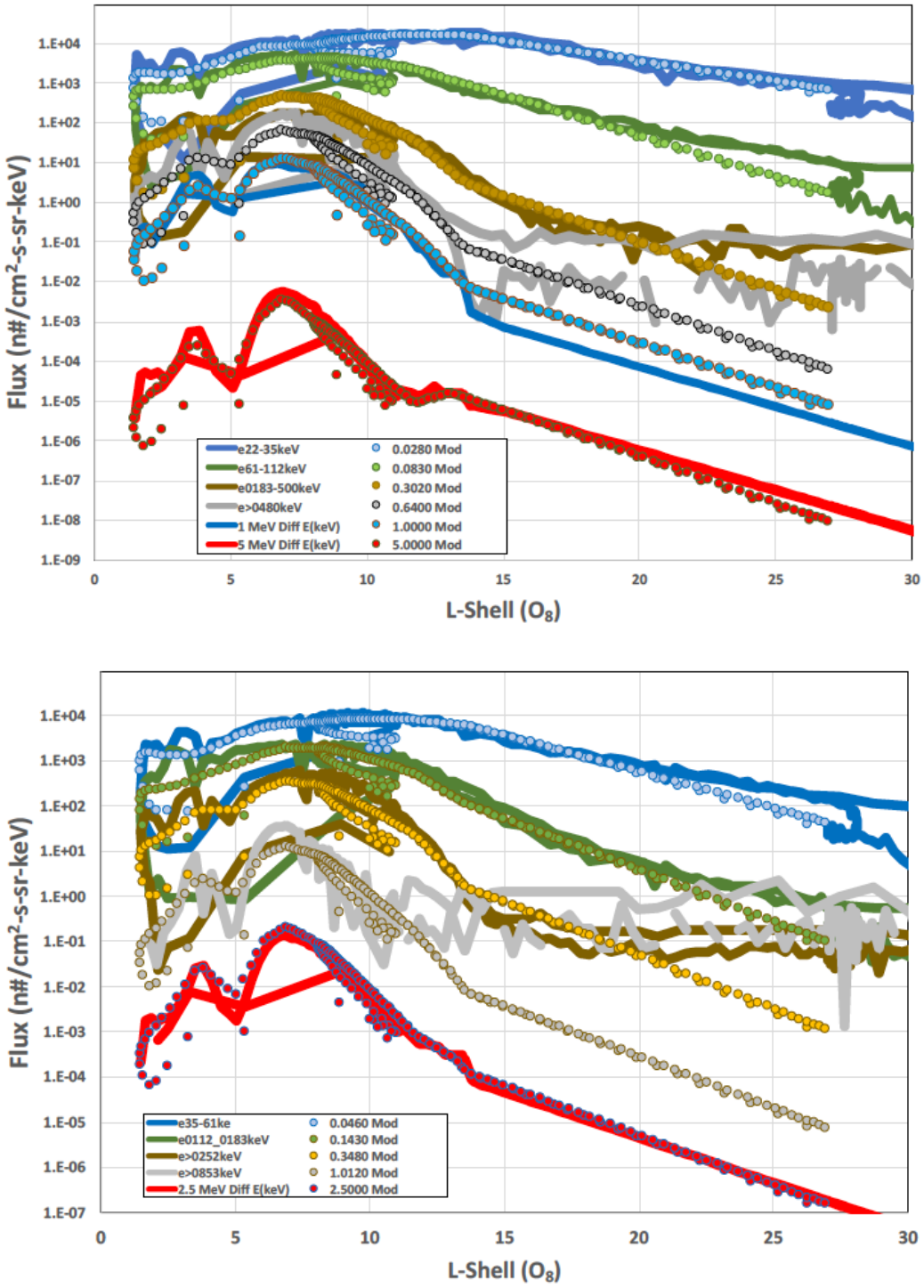

Figure 19. Electron flux data versus L-shell (O_8) from the PDS for the specified energies compared with the NMOD model fluxes. The top and bottom charts show alternating energy ranges for clarity.

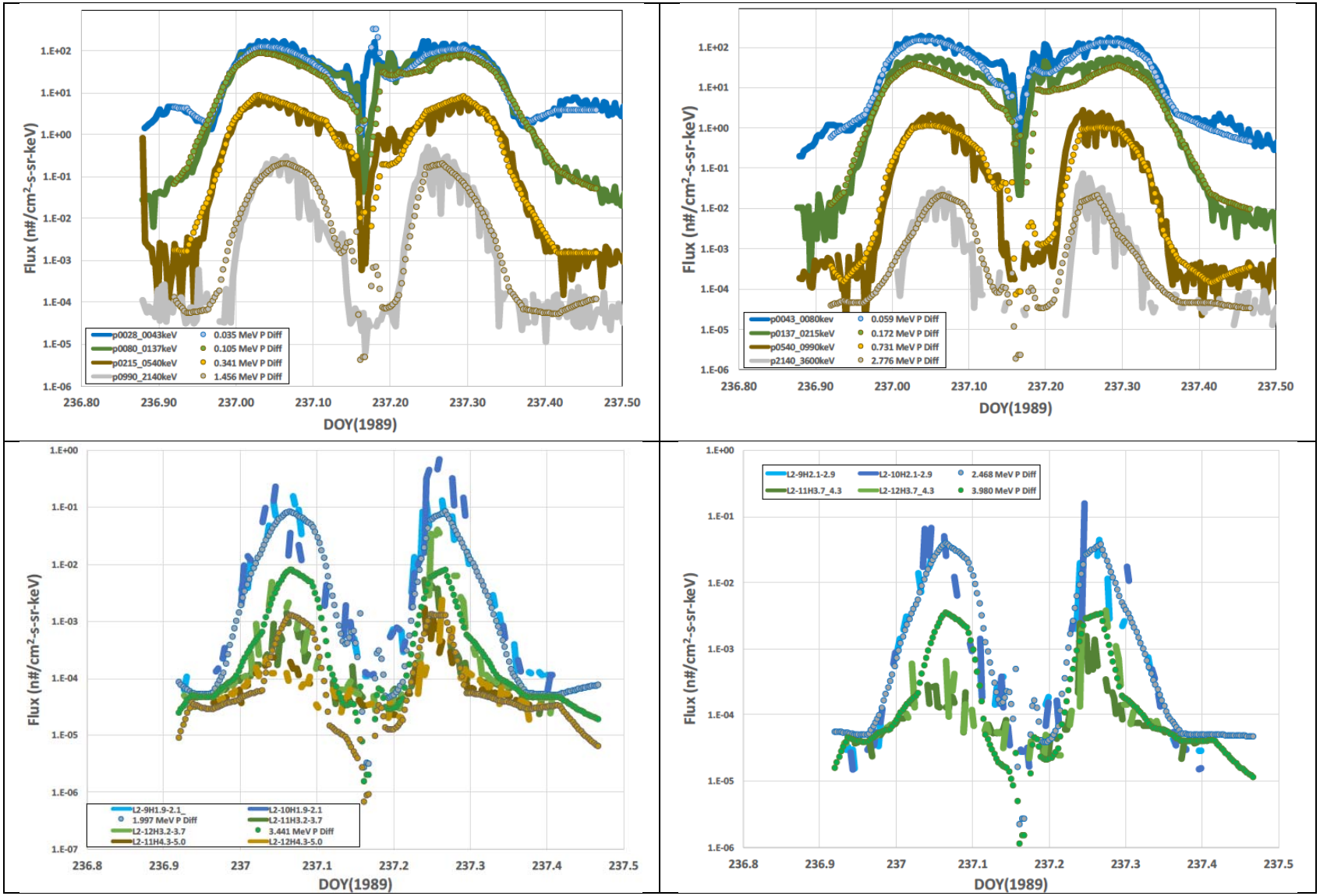

Figure 20. Proton flux data versus time from the PDS for the specified energies compared with the NMOD model fluxes. The left and right charts show alternating energy ranges for clarity.

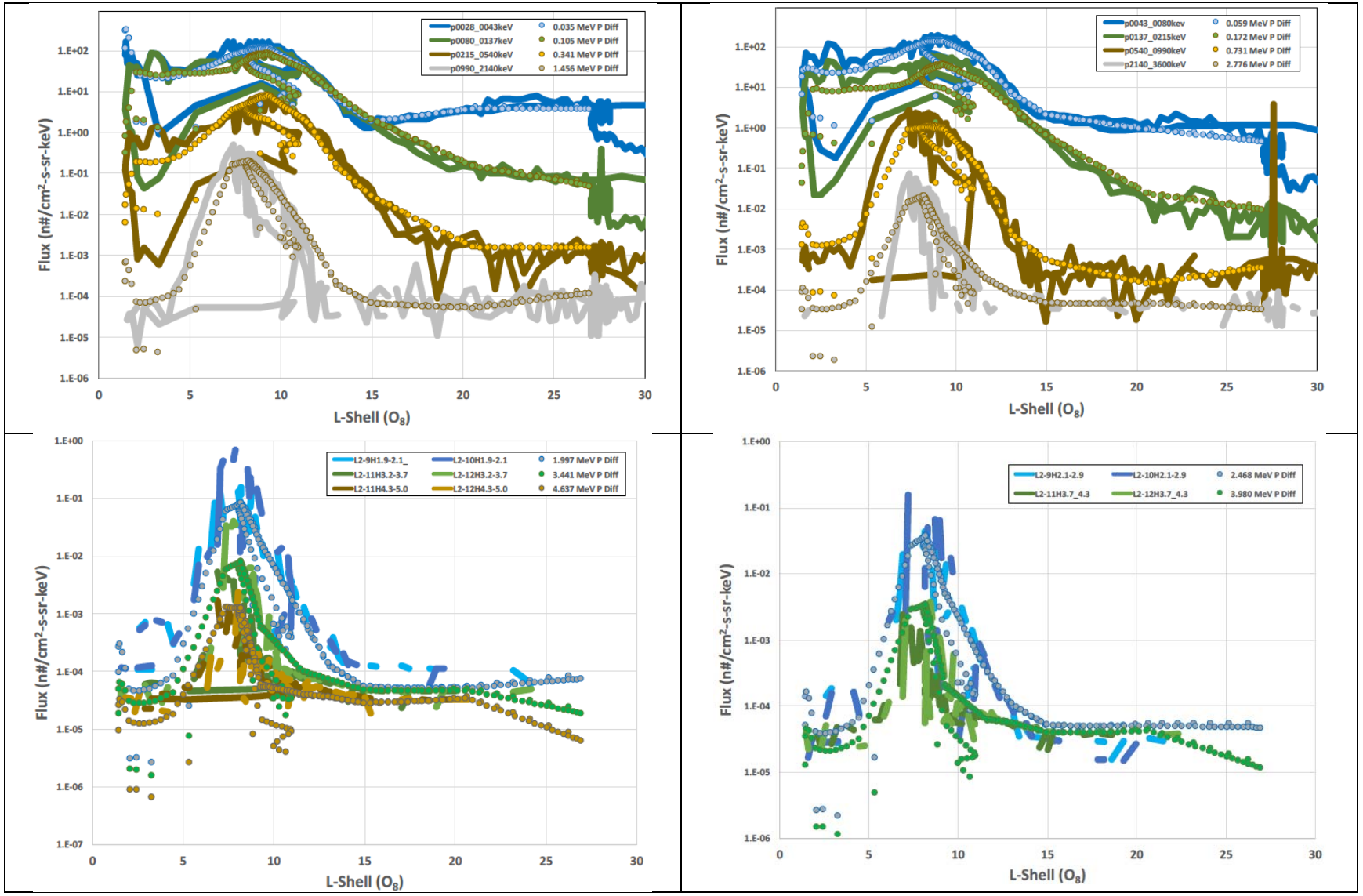

Figure 21. Proton flux data versus L-shell (O_8) from the PDS for the specified energies compared with the NMOD model fluxes. The left and right charts show alternating energy ranges for clarity.

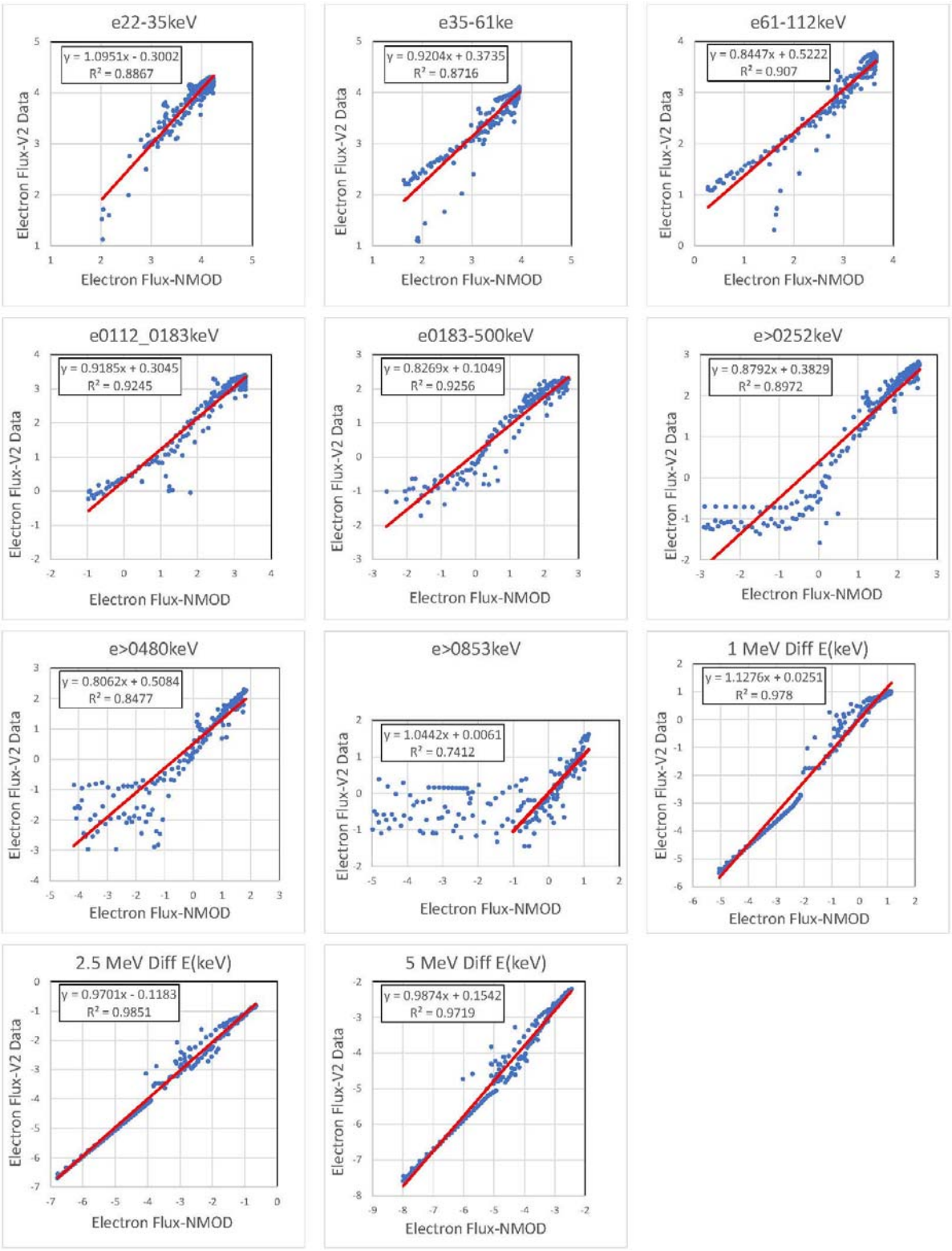

Figure 22. Linear correlations for the electrons between the PDS data and the NMOD model predictions. The regressions are carried out for the Log_{10} of the fluxes in all cases.

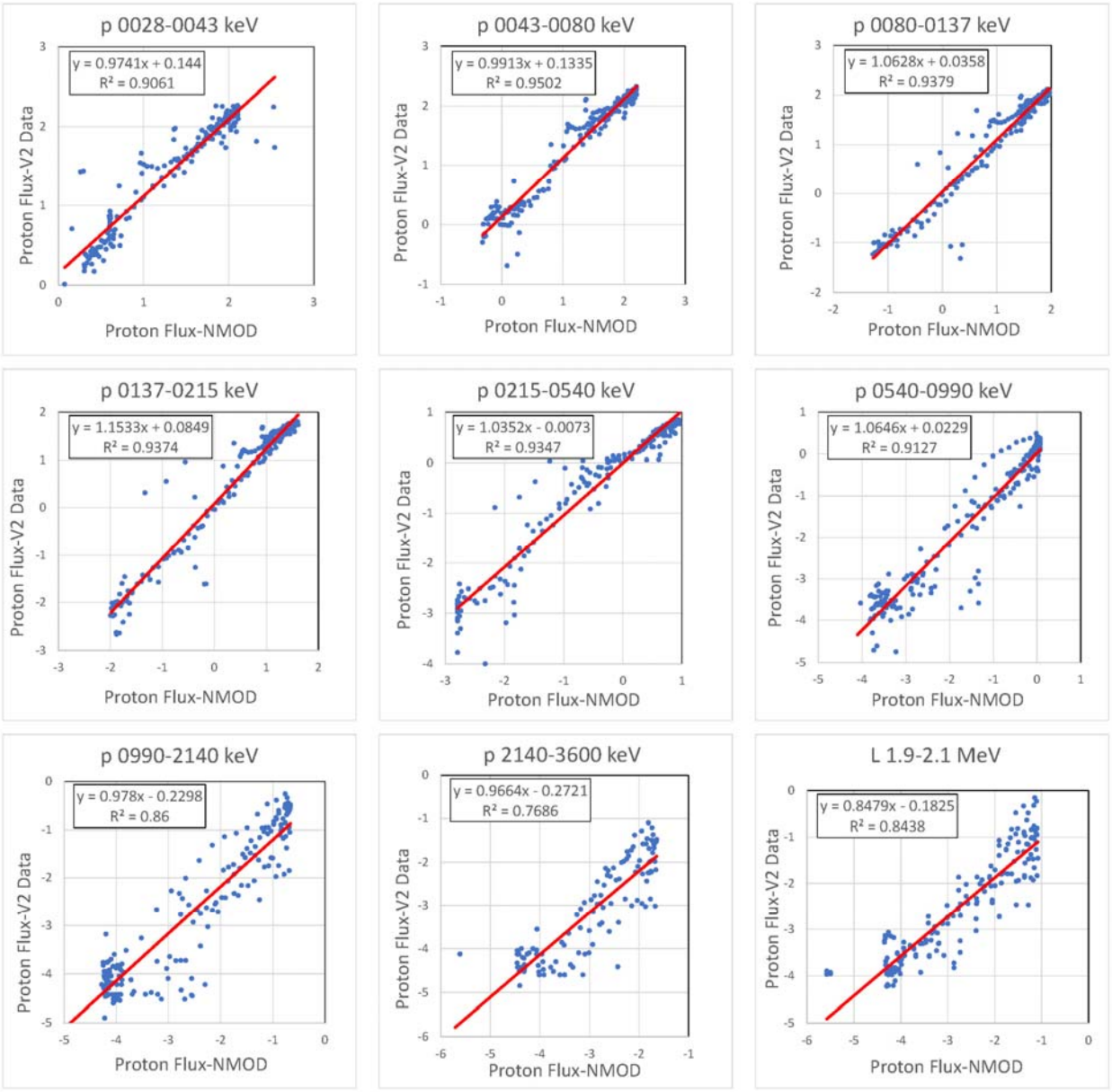

Figure 23. Linear correlations for the protons between the PDS data and the NMOD model predictions. The regressions are carried out for the Log_{10} of the fluxes in all cases.

(1 of 2)

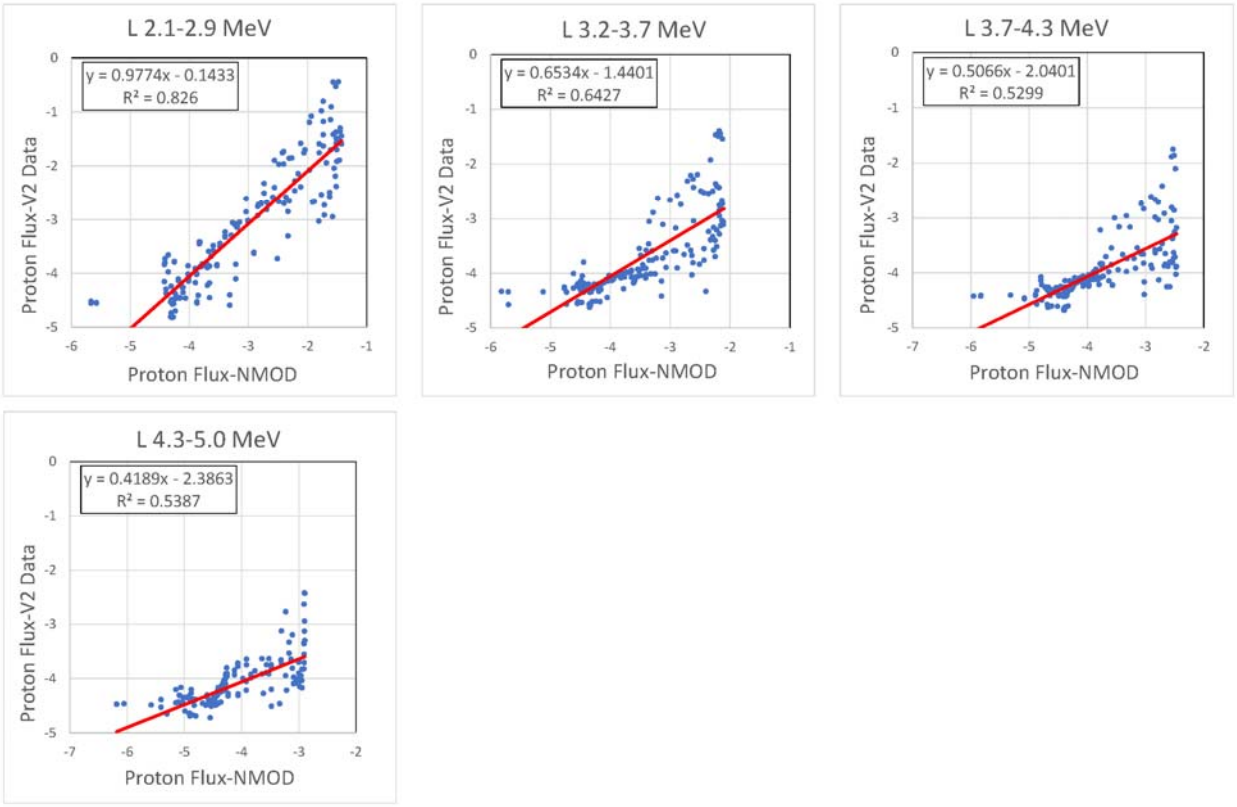

Figure 23. Linear correlations for the protons between the PDS data and the NMOD model predictions. The regressions are carried out for the Log_{10} of the fluxes in all cases. (2 of 2)

The cross-correlation results quantitatively confirm the previous observations about the time and L-shell comparisons. In particular, the linear regressions of Log_{10} of the electron data fluxes versus the Log_{10} of the model fluxes show very high correlations coefficients across the entire energy range (note: for the electron channel 0.853–1.2 MeV, the fit was only for model fluxes from –1 up so as to remove the background noise in the data which would skew the fit). As observed earlier, the proton data are not as well correlated with the model predictions at the three highest energies. If the regression fit coefficients are interpreted (based on a Log_{10} linear regression fit which gives $y(Log_{10}(data)) = A(Log_{10}(model)) + B$ in Tables 9 and 10) to give "Data ~ $10^{B}Model^{A}$", as "A" is ~1 in almost all cases, the electron predictions are within a factor of 2 to 3 of the PDS data (i.e., $0.3 < 10^{B} < 3.0$). The proton fits give similar results except for the three highest channels, which can exhibit order-of-magnitude variations (i.e., $10^{B} < 0.1$). As noted earlier, more effort in the future needs to be addressed towards improving the proton fits at energies above 3 MeV.

Table 9. Cross-correlations between the LECP PDS and CRS LET proton data and the NMOD predictions for the indicated energy intervals. Listed are the correlation coefficients, R^2, and the linear fits to the Log_{10} flux values (x = log_{10}(NMOD), y = log_{10}(PDS)).

E0 (MeV)	E1 (MeV)	Geo Mean	Correlation Coefficient	Fit to Log_{10} Values
0.028	0.043	0.035	R^2 = 0.90612	y = 0.9741x + 0.144
0.043	0.080	0.059	R^2 = 0.95018	y = 0.9913x + 0.1335
0.080	0.137	0.105	R^2 = 0.93794	y = 1.0628x + 0.0358
0.137	0.215	0.172	R^2 = 0.93737	y = 1.1533x + 0.0849
0.215	0.540	0.341	R^2 = 0.93467	y = 1.0352x - 0.0073
0.540	0.990	0.731	R^2 = 0.9127	y = 1.0646x + 0.0229
0.990	2.140	1.456	R^2 = 0.85998	y = 0.978x - 0.2298
2.140	3.600	2.776	R^2 = 0.76862	y = 0.9664x - 0.2721
1.900	2.100	1.997	R^2 = 0.8438	y = 0.8479x - 0.1825
2.100	2.900	2.468	R^2 = 0.82598	y = 0.9774x - 0.1433
3.200	3.700	3.441	R^2 = 0.64266	y = 0.6534x - 1.4401
3.700	4.300	3.989	R^2 = 0.52986	y = 0.5066x - 2.0401
4.300	5.000	4.637	R^2 = 0.53866	y = 0.4189x - 2.3863

Table 10. Cross-correlations between the LECP PDS and CRS TET electron data and the NMOD predictions for the indicated energy intervals. Listed are the correlation coefficients, R^2, and the linear fits to the Log_{10} flux values (x = log_{10}(NMOD), y = log_{10}(PDS)).

E0 (MeV)	E1 (MeV)	Geo Mean	Correlation Coefficient	Fit to Log_{10} Values
0.022	0.035	0.028	R^2 = 0.88665	y = 1.0951x - 0.3002
0.035	0.061	0.046	R^2 = 0.87159	y = 0.9204x + 0.3735
0.061	0.112	0.083	R^2 = 0.90695	y = 0.8447x + 0.5222
0.112	0.183	0.143	R^2 = 0.92445	y = 0.9185x + 0.3045
0.183	0.500	0.302	R^2 = 0.92558	y = 0.8269x + 0.1049
0.252	0.480	0.348	R^2 = 0.89719	y = 0.8792x + 0.3829
0.480	0.853	0.640	R^2 = 0.84766	y = 0.8062x + 0.5084
0.853	1.200	1.012	R^2 = 0.74116	y = 1.0442x + 0.0061
1.000	1.000	1.000	R^2 = 0.97799	y = 1.1276x + 0.0251
2.000	2.000	2.000	R^2 = 0.98505	y = 0.9701x - 0.1183
5.000	5.000	5.000	R^2 = 0.97188	y = 0.9874x + 0.1542

10. Applications of NMOD

Figure 24 illustrates a simple application of the NMOD model for mission planning—a plot of the 1 MeV electron integral flux and the 5 MeV proton integral flux contours for a meridian projection (idealized dipole coordinates R-λ). 1 MeV electrons and 5 MeV protons are roughly the cutoff energies for 50–100 mils of aluminum shielding, nominal shielding levels for a typical spacecraft design point. Clearly the region outside around 8–10 R_N should be very safe for total ionizing dose (TID) if that is a mission concern. Similarly, the NMOD can be used for the traditional purpose of modeling the TID for a spacecraft flyby. To be specific, Fig. 25 is a graph of the estimated TID rate as a function of distance in L along the equator. For 100 mils of aluminum shielding, the maximum total dose is on the order of only 1000 rad(Si) after 100 days, an insignificant amount for a mission in comparison to a single flyby of Jupiter. While orbital missions to Neptune will clearly see radiation, the NMOD indicates that radiation will likely not be a serious concern for mission designers if standard 100 mil aluminum shielding or similar shielding design procedures are followed.

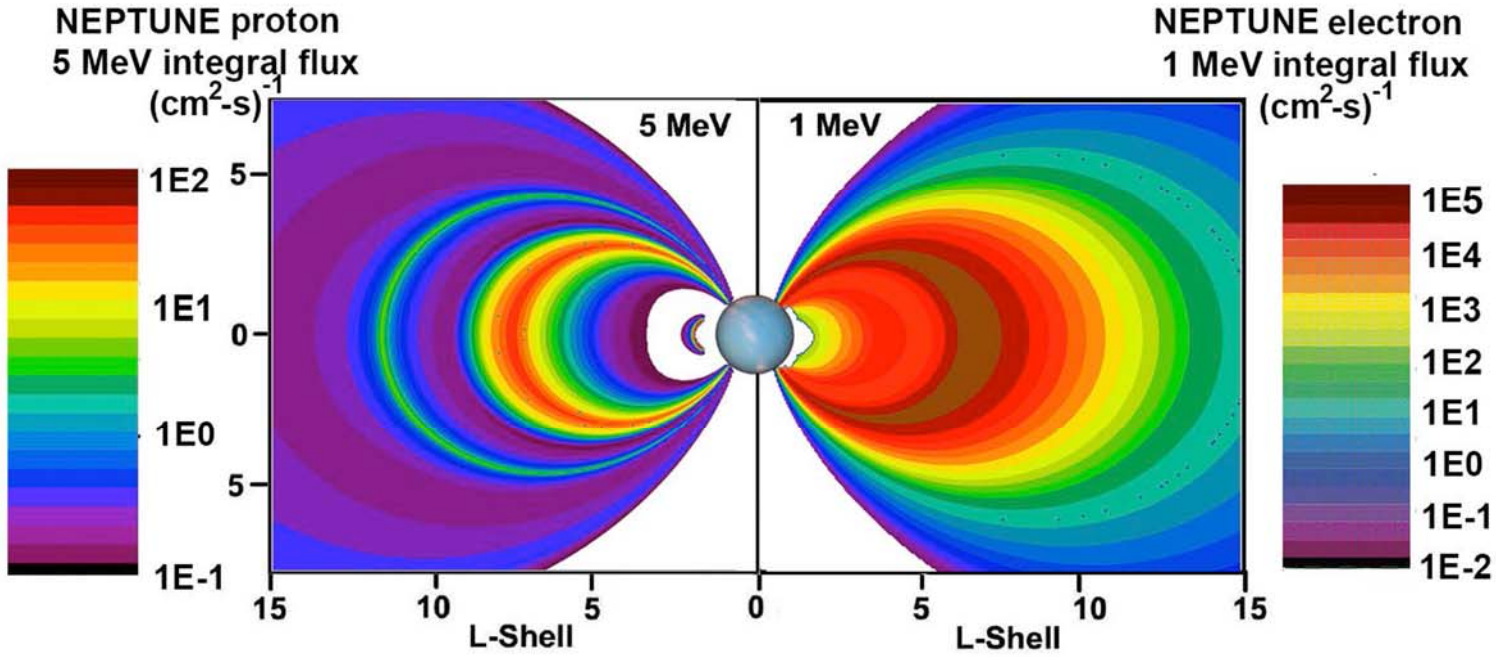

Figure 24. A plot of the 1-MeV electron and 5-MeV proton fluxes for a meridian profile (e.g., idealized dipole coordinates R-λ) of the Neptunian radiation belts. Note that there is an absence of data inside 1.5 R_N—this does not represent the absence of radiation flux in this region!

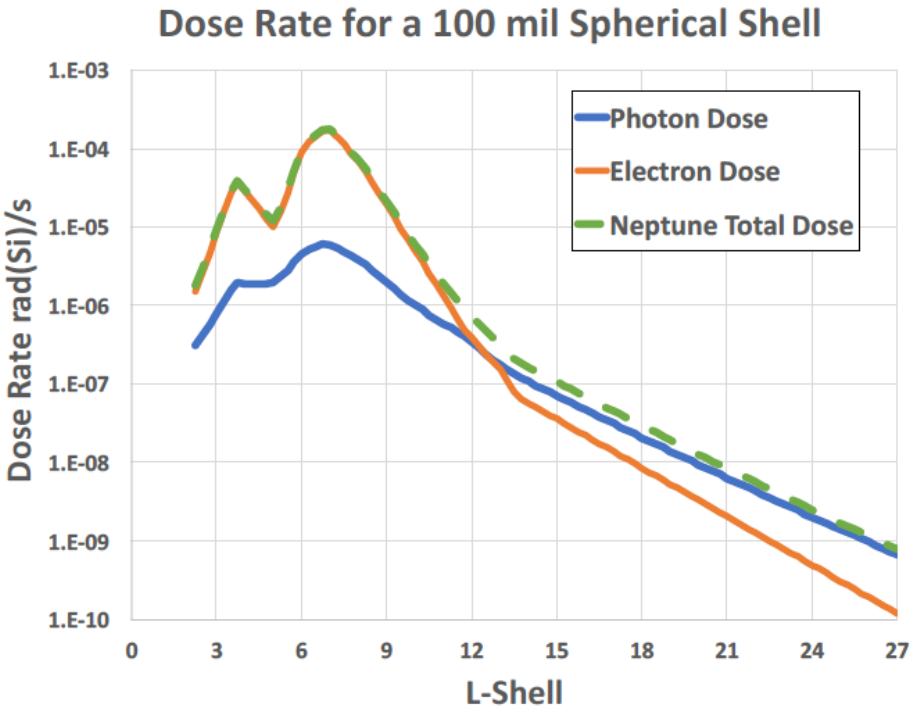

Figure 25. Graph of the estimated total ionizing dose rate (rad(Si)/s) versus L-shell based on the NMOD radiation model.

11. Conclusion

The preceding has outlined the development of the NMOD Neptunian radiation model. As a first step, various OTD magnetic field models were compared with a more complex "Schmidt-Normalized" coefficient model called "O_8" (Connerney, 1991). The latter model was then used to compute B-L components for Neptune. A parametric fit to the electron and proton spectra at fixed locations in L-shell was then translated into a FORTRAN code that takes B-L coordinates and computes the omnidirectional differential and integral electron fluxes. The resulting NMOD radiation model covers the range from ~0.022 MeV up to ~5.0 MeV for the electrons and from ~0.028 MeV to ~5.0 MeV for the protons. The complete data set derived from the PDS and the literature was then used to test the electron and proton model predictions. The NMOD model was found to be within a factor of ~2–3 for the electrons and for the protons (except at energies above 3 MeV). The final product is in the form of a FORTRAN program capable of predicting the magnetic field and the electron and proton radiation environments along an arbitrary trajectory. The complete package is included as Appendix A3 of JPL IOM 5130-17-007 [Garrett and Evans, 2017]. Two useful applications of the model were presented that illustrate the intricate and complex radiation belt structure of the Neptunian radiation belts. The NMOD is now ready for mission design applications and for further testing and improvement.

References

Acuna, M. H., J. E. P. Connerney, and N. F. Ness, "Neptune's Magnetic Field' Calculation of Field Geometric Invariants Derived from the I8E1 GSFC/BRI Model," *J. Geophys. Res.*, vol. 98, no. A7, pp. 11,275–11,284, July 1, 1993.

Bagenal, F., "Giant Planet Magnetospheres," *Ann. Rev. Earth Planet. Sci.*, vol. 20, pp. 289–328, 1992.

Connerney, J. E. P., M. H. Acuna, and N. F. Ness, "The Magnetic Field of Neptune," *J. Geophys. Res.*, vol. 92, no. A13, pp. 15,329–15,336, Dec. 30, 1987.

Connerney, J. E. P., M. H. Acuna, and N. F. Ness, "The Magnetic Field of Neptune," *J. Geophys. Res.,* Vol. 96, Supplement, pp. 19,023–19,042, Oct. 30, 1991.

Connerney, J. E. P., "Magnetic Fields of the Outer Planets," *J. Geophys. Res.*, vol. 98, no. E10, pp. 18,659–18,679, Oct. 25, 1993.

Evans, R., *PDS and Modern Neptune Co-ordinates*, IOM 5132-13-007 (also D-95199) (internal document), Jet Propulsion Laboratory, California Institute of Technology, Pasadena, CA, Jan. 21, 2013.

Evans, R. W., *DPS and Modern Neptune Coordinates and Neptune Magnetic Field models*, IOM 5132-2017-015 (internal document), Jet Propulsion Laboratory, California Institute of Technology, Pasadena, CA, June 14, 2017a.

Evans, R. W., *DPS and Published Neptune Data for Energetic Particles*, IOM 5132-2017-016 (internal document), Jet Propulsion Laboratory, California Institute of Technology, Pasadena, CA, June 14, 2017b.

Garrett, H. B., L. M. Martinez-Sierra, and R. W. Evans, *The JPL Uranian Radiation Model (UMOD)*, JPL Publication 15-7, California Institute of Technology, Pasadena, CA, pp. 55, Sept. 2015.

Garrett, H. B., and R. W. Evans, *NMOD Radiation Model Description and FORTRAN Code*, IOM 5130-17-007 (internal document), Jet Propulsion Laboratory, California Institute of Technology, Pasadena, CA, July 1, 2017.

Hofstdater, M., A. Simon, K. Reh, and J. Elliott, *Ice Giants Pre-Decadal Study Final Report*, prepared by the Solar System Exploration Directorate, Jet Propulsion Laboratory, for the NASA Planetary Science Division, JPL D-100520, Jet Propulsion Laboratory, California Institute of Technology, Pasadena, CA, June 2017. http://www.lpi.usra.edu/icegiants/mission_study/Full-Report.pdf

Looper, M. D., "Energetic Protons in the Magnetosphere of Neptune," Doctoral Thesis, California Institute of Technology, Pasadena, CA, Jan. 8, 1993.

Mauk, B. H., S. M. Krimigis, E. P. Keath, A. F. Cheng, T. P. Armstrong, L. J. Lanzerotti, G. Gloeckler, and D. C. Hamilton, "The Hot Plasma and Radiation Environment of the Neptunian Magnetosphere," *J. Geophys. Res.*, vol. 92, no. A13, pp. 15,283–15,308, Dec. 30, 1987.

Mauk, B. H., E. P. Keath, M. Kane, S. M. Krimigis, A. F. Cheng, M. H. Acuna, T. R Armstrong, and N. F. Ness, "The Magnetosphere of Neptune: Hot Plasmas and Energetic Particles", *J. Geophys. Res*., vol. 96, Supplement, pp. 19,061–19,084, Oct. 30, 1991.

Mauk, B.H., S. M. Krimigis, and M. H. Acuna, "Neptune's inner magnetosphere and aurora: Energetic particle constraints, *J. Geophys. Res*., vol. 99, no. A8, Pages 14,781–14,788, Aug. 1, 1994.

Mauk, B. H., S. M. Krimigis, A. F. Cheng, and R. S. Selesnick, "Energetic Particles and Hot Plasmas of Neptune," in *Neptune and Triton*, edited by D. P. Cruikshank, M. S. Matthews, and A. M. Schumann, the University of Arizona press, pp 169–232, 1995.

Ness, N. F., M. H. Acuna, L. F. Burlaga, J. E. P. Connerney, R. P. Lepping, and F. M. Neubauer, "Magnetic Fields at Neptune," *Science*, vol. 246, pp. 1473–1477, Dec. 15 1989.

Ness, N. F., M. Acuna, and J. E. P. Connerney "Neptune's Magnetic Field and Field Geometric Properties," in *Neptune and Triton*, edited by D. P. Cruikshank, M. S. Matthews, and A. M. Schumann, University of Arizona Press, pp. 141–168, 1996.

Selesnick, R. S., and E. C. Stone, "Energetic electrons at Uranus: Bimodal Diffusion in a Satellite Limited Radiation Belt," *J. Geophys. Res.*, vol. 96, no. A4, pp. 5651–5665, April 1, 1991.

Selesnick, R. S., and E. C. Stone, "Energetic Particle Signatures of Satellites and Rings in Neptune's Magnetosphere," *Adv. Space Res.*, vol.12, no.11, pp. (11)71—(11)79, 1992.

Smith, B. A., L. A. Soderblom, D. Banfield, C. Barnet, A. T. Basilevsky, R. F. Beebe, K. Bolinger, J. M. Boyce, A. Brahic, G. A. Briggs, R. H. Brown, C. Chyba, S. A. Collins, T. Colvin, A. F. Cook II, D. Crisp, S. K. Croft, D. Cruikshank, J. N. Cuzzi, G. E. Danielson, M. E. Davies, E. De Jong, L. Dones, D. Godfrey, J. Goguen, I. Grenier, V. R. Haemmerle, H. Hammel, C. J. Hansen, C. P. Helfenstein, C. Howell, G. E. Hunt, A. P. Ingersol, T. V. Johnson, J. Kargel, R. Kirk, D. I. Kuehn, S. Limaye, H. Masursky, A. McEwen, D. Morrison, T. Owen, W. Owen, J. B. Pollack, C. C. Porco, K. Rages, P. Rogers, D. Rudy, C. Sagan, J. Schwartz, E. M. Shoemaker, M. Showalter, B. Sicardy, D. Simonelli, J. Spencer, L. A. Sromovsky, C. Stoker, R. G. Strom, V. E. Suomi, S. P. Synnott, R. J. Terrile, P. Thomas, W. R. Thompson, A. Verbiscer, and J. Veverka, "Voyager 2 in the Neptunian System: Imaging Science Results," *Science*, vol. 246, pp. 1422–1449, Dec. 15, 1989.

Stone, E. C., R. E. Vogt, F. B. McDonald, B. J. Teegarden, J. H. Trainor, J. R. Jokipii, and W. R. Webber, "Cosmic ray investigation for the Voyager missions: Energetic particle studies in the outer heliosphere and beyond", *Sp. Sci. Rev.*, vol. 21, pp 355–, 1977.

Stone, E. C., A. C. Cummings, M. D. Looper, R. S. Selesnick, N. Lal, F. B. McDonald, J. H. Trainor, and D. L. Chenette, "Energetic Charged Particles in the Magnetosphere of Neptune," *Science*, vol. 246, pp. 1490–1494, Dec. 11, I989.

Vision and Voyages for Planetary Science in the Decade 2013-2022, National Academy of Sciences, Washington, D.C., 2011.

Warwick, J. W., D. R. Evans, G. R. Peltzer, R. G. Peltzer, J. H. Romig, C. B. Sawyer, A. C. Riddle, A. E. Schweitzer, M. D. Desch, M. L. Kaiser, W. M. Farrell, T. D. Carr, I. De Pater, D. H. Staelin, S. Gulkis, R. L. Poynter, A. Boischot, F. Genova, Y. Leblanc, A. Lecacheux, B.

M. Pedersen, and P. Zarka, "Voyager Planetary Radio Astronomy at Neptune," *Science*, vol. 246, pp. 1498–1501, Dec. 15 1989.

Appendix A1. Fits to the Neptune Differential Intensity Spectra at selected L-shells

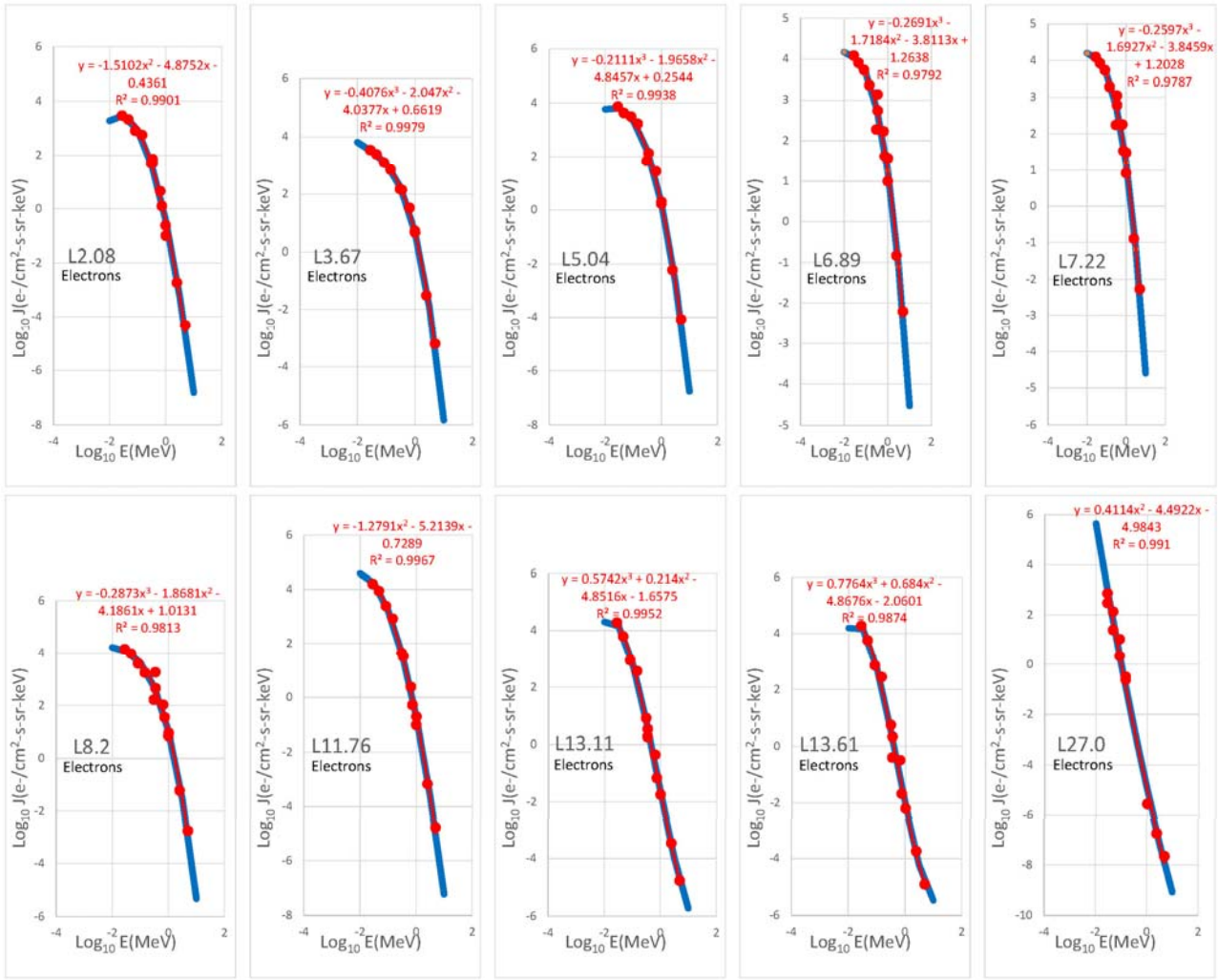

Figure A1-1. Polynomial fits (blue) in terms of the Log_{10} of the energy to the original Neptune database (red) electron differential intensity spectra at the indicated L-shells.

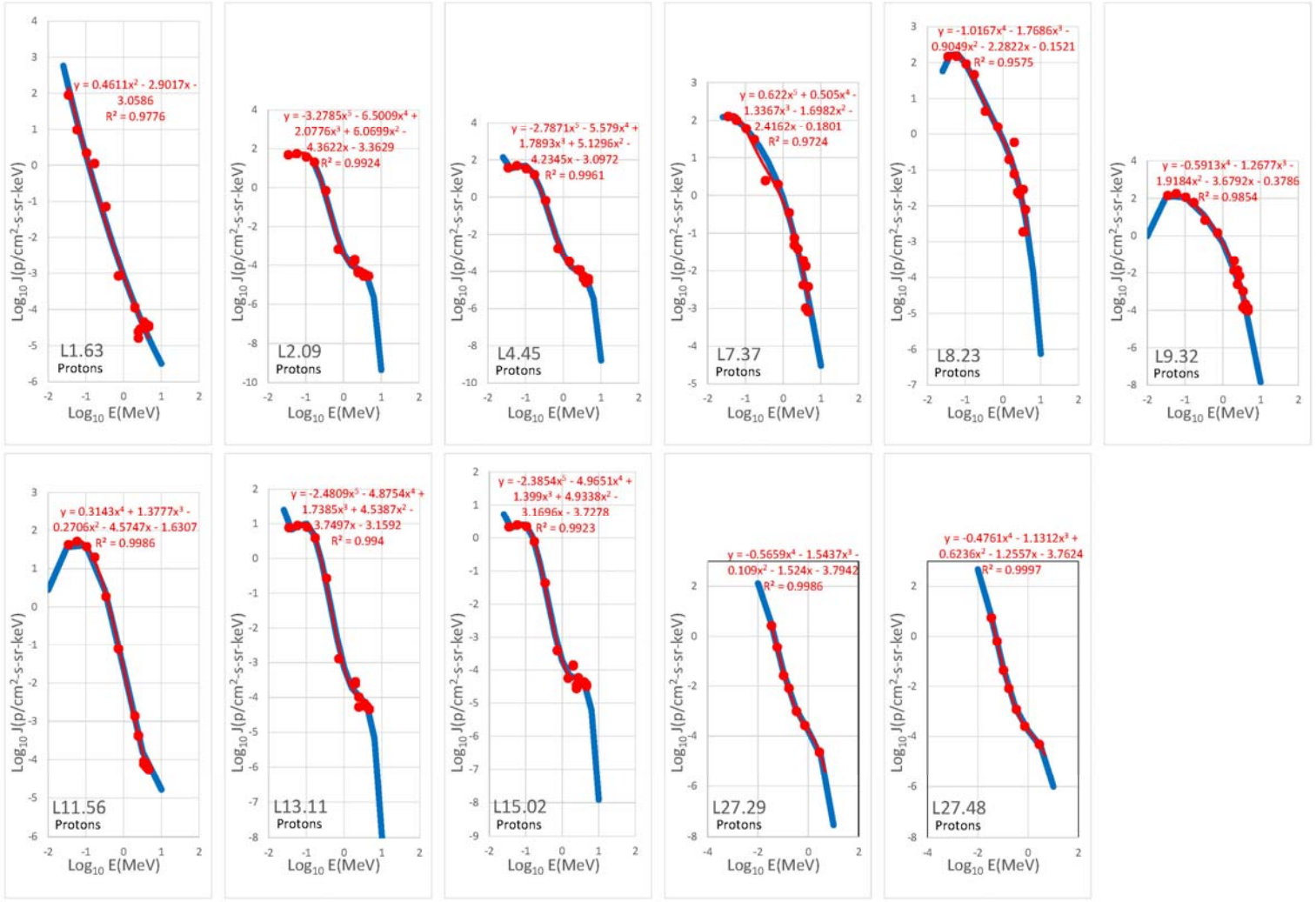

Figure A1-2. Polynomial fits (blue) in terms of the Log_{10} of the energy to the original Neptune database (red) proton differential intensity spectra at the indicated L-shells.

Appendix A2. Acronyms, Abbreviations, and Terms

Ao	constant for defining particle spectra (Eq. 1)
APL	Johns Hopkins University Applied Physics Laboratory
B	magnetic field strength (general)
B_{eq}	magnetic field at the equator
B_{sc}	magnetic field at the spacecraft
B-L	magnetic field coordinates of a point
B(PDS)	magnetic field data from the PDS
CR	count rate
CRS	Cosmic Ray Subsystem (on Voyager 2)
CTS	counts per second
dE	delta energy change
DP	simple dipole model developed by Ness et al. [1996]
GEO	geometric mean energy
IAU	International Astronomical Union
J2000	international standard for starting time referencing noon, Jan. 1, 2000
JHU	Johns Hopkins University
L	the magnetic L-shell parameter; distance in planetary radii at which a magnetic field line crosses the magnetic equator
LECP	Low Energy Charged Particle Detector (on Voyager 2)
LET	Low Energy Telescopes (on Voyager 2)
N	Neptune
NAIF	(NASA) Navigation and Ancillary Information Facility
NMOD	Neptune Radiation Model

O_8	multi-pole expansion model
OTD	Offset Tilted Dipole magnetic field model
PDS	Planetary Data System
PHA	pulse height analyzer
PHI	east longitude
R^2	regression coefficient
RA	right ascension
RMS, rms	root mean square
R_N	Neptunian radius, 24,764 km
SCET	Spacecraft Event Time
Sqrt	square root

SPICE

- S- Spacecraft ephemeris, given as a function of time. (SPK)
- P- Planet, satellite, comet, or asteroid ephemerides, or more generally, location of any target body, given as a function of time. (also SPK)
- The P kernel also logically includes certain physical, dynamical and cartographic constants for target bodies, such as size and shape specifications, and orientation of the spin axis and prime meridian. (PCK)
- I- Instrument description kernel, containing descriptive data peculiar to a particular scientific instrument, such as field-of-view size, shape and orientation parameters. (IK)
- C- Pointing kernel, containing a transformation, traditionally called the "C-matrix," which provides time-tagged pointing (orientation) angles for a spacecraft bus or a spacecraft structure upon which science instruments are mounted. A C-kernel may also include angular rate data for that structure. (CK)
- E- Events kernel, summarizing mission activities - both planned and unanticipated. Events data are contained in the SPICE EK file set, which consists of three components: Science Plans, Sequences, and Notes. (EK))

TET	"The Electron Telescope" on Voyager 2
TID	total ionizing dose
UT	Universal Time